Aeroacoustic Analysis of a Wind Turbine with Sinusoidal Leading-Edge Blade

By

Vinay Valleru

Submitted to the graduate degree program in Aerospace engineering and the Graduate Facility of The University of Kansas in partial fulfillment of the requirements for the degree of Master of Science.

Dr. Ray Taghavi, Chairperson

Dr. Saeed Farokhi, Committee Member

Dr. Huixuan Wu, Committee Member

Date Defended: 10/01/2018

The Thesis Committee for Vinay Valleru
certifies that this is the approved version of the following thesis:

Aeroacoustic Analysis of a Wind Turbine with Sinusoidal Leading-Edge Blade

Dr. Ray Taghavi, Chairperson

Dr. Saeed Farokhi, Committee Member

Dr. Huixuan Wu, Committee Member

Date Defended: 10/01/2018

Abstract

Wind turbines are a major source of renewable power generation in the U.S with a share of 4.7% in total electricity produced and is a clean energy source. While wind energy has its advantages, it also has room for improvement and few drawbacks. One of the drawbacks is the noise associated with the operation of the wind turbine and its impact on nearby communities. The noise generated from wind turbines is known to cause annoyance and sleep disturbance to the people living nearby and few countries have acted to regulate the installation of wind turbines near communities.

The primary aim of this research is to design a wind turbine blade with tubercles and evaluate it's aerodynamic and noise performance. A preliminary step in achieving this goal is to perform 3D steady flow analysis and noise analysis on a base model, namely the NREL Phase VI blade using commercial CFD software, STAR CCM+. Three-dimensional steady RANS equations with SST k-ω turbulence model with all y^+ wall treatment is used to perform numerical analysis of the blade at five different wind speeds from 7m/s to 25m/s, by keeping the wind turbine angular speed constant at 72RPM. To reduce computational cost and time, only one blade is analyzed instead of two, and a periodic boundary condition is used with 180^0 symmetry. The pressure data from the CFD results are used as an input to Curle Broadband Noise source model to estimate the sound Pressure level (SPL).

This process aids in validating the prediction that the bionic wind turbine blade can be more efficient and generate less noise than a conventional wind turbine at the same wind speeds.

Acknowledgements

I would like to extend my gratitude to Dr. Ray Taghavi who provided me the topic of this study and constantly guided me with ideas and solutions all throughout this research. I would also like to thank him for all his invaluable guidance that I received throughout my Master's program. I would like to thank Dr. Saeed Farokhi and Dr. Huixuan Wu for providing me with valuable inputs and taking time to review this thesis and providing comments and suggestions.

I would like to thank Mohit Nahar and Rohith Giridhar for their constant support throughout my thesis.

I would also like to thank my family whose constant love, encouragement and support helped me complete my Master's thesis.

Table of Contents

List of Figures

List of Tables

Nomenclature

Latin Letters

c_o ..... Local chord length of blade ..... m

a_0 ..... Speed of sound ..... m/s

Cp ..... Coefficient of pressure ..... -

CT ..... Coefficient of Torque ..... -

f ..... Frequency of flow disturbance ..... Hz

I ..... Intensity of sound transmission ..... W/m^2

R ..... Blade span ..... m

L_p ..... Sound Pressure Level ..... dB

L_w ..... Sound Power Level..... dB

M……Mach Number…..……. -

$\dot{m}$ ..... Mass flow rate ..... kg/s

n..... Number of rotor blades ..... ~

p..... Local static pressure ..... Pa

p_α..... Ambient pressure ..... Pa

r ..... Local radius of rotation of the blade..... m

T ..... Torque generated by wind turbine ..... Nm

v..... Wind Velocity ..... m/s

u, v, w……. Velocity Components…….m/s

Greek Letters

λ ..... wavelength of flow disturbance ..... m

κ ……..….Turbulent Kinetic Energy……...……. -

ε……Turbulent Dissipation rate…… -

ω…….Specific Dissipation rate……. -

ρ ..... density .....kg/m^3

θ_p..... blade pitch angle ..... deg

ω ..... angular velocity of blade rotation ..... rad/s

Abbreviations

CFD	Computational Fluid Dynamics
FW-H	Ffowcs Williams and Hawkings
FFT	Fast Fourier Transform
IDDES	Improved Delayed Detached Eddy Simulation
HAWT	Horizontal Axis Wind Turbine
LES	Large Eddy Simulation
NREL	National Renewable Energy Laboratory
OASPL	Overall Sound Pressure Level
RANS	Reynolds-Average Navier Stokes
SPL	Sound Pressure Level
URANS	Unsteady RANS
TKE	Turbulent Kinetic Energy
SST	Shear Stress Transport
GW	Giga Watt
MW	Mega Watt
KW	Kilo Watt
UAE	Unsteady Aerodynamic Experiment
3D	Three Dimensional
RPM	Rotations Per Minute
NASA	National Aeronautics and Space Agency
LE	Leading Edge
TE	Trailing Edge
CAD	Computer Aided Drawing
VAWT	Vertical Axis Wind Turbine

1. Introduction

Humpback whale is unique among the whales for its ability to do extraordinary maneuvers underwater to catch a prey. Various experiments conducted by Fish and Battle (1995) on the whale species has identified that this maneuvering capability is achieved due to the presence of tubercles or protuberances on the whale flipper. It is understood that presence of tubercles can effectively delay the stall angle by 40% while with a 6% increase in lift and 32% reduction in drag [1] [2]. To take advantage of this better stall performance, many efforts have been made to mimic the whale flipper to the advantage of wind turbines in generating more power at high wind speed flows. Some results have revealed that this kind of wind turbine blade can perform more stable, quiet and capture more wind energy than the conventional blades [3] [4].

It is observed that the efficiency of the sinusoidal leading edge depends on the wavelength and amplitude. [5] [6] [7] To reduce the cost of computation, a sinusoidal leading edge design with proven performance improvement is selected from Ref. [5] for this research. The blade has an amplitude of $0.025c_o$ and a wavelength of $0.25c_o$ where max chord, c_o=0.737m.Wind turbines are a major source of power generation in the U.S with a share of 4.7% in total electricity produced [8] and is a clean energy source. While wind energy has its advantages, it has few drawbacks and one of them is the noise associated with the operation of the wind turbine. The noise generated from wind turbines is known to cause annoyance and sleep disturbance to the people living nearby

[9] and few countries have taken action to regulate the installation of wind turbines near communities. [10] The main aim of this research is to design a wind turbine blade with tubercles and evaluate it's aerodynamic and Dipole noise performance using Curle broadband noise model. A preliminary step in achieving this goal is to perform 3D Steady flow analysis and noise analysis on a base model-an NREL Phase VI blade using commercial CFD software, STAR CCM+. Three-dimensional Steady RANS equations SST k-ω turbulence model with all y^+ wall treatment is used to perform numerical analysis of the blade at five different wind speeds from 7m/s to 25m/s, by keeping the wind turbine speed constant at 72RPM. To reduce computational cost and time, only one blade is analyzed instead of two, and a periodic boundary condition is used with 180^0 symmetry.

1.1. Unsteady aerodynamic experiment Phase VI

Since 1987, National Renewable Energy Laboratory (NREL) has been conducting experiments at National Wind Technology Center (NWTC) near Golden, Colorado to understand the three-dimensional aerodynamic behavior of Horizontal Axis Wind Turbines (HWAT). All the wind turbine codes during this time are based on aerodynamic forces derived from two-dimensional airfoil tests. But the field tests conducted by NREL and similar tests in Europe revealed that wind turbines in a field environment undergo very complex aerodynamic behavior. Field studies have shown that 3-D effects are very prevalent in wind turbine operation and additionally, wind turbines are subjected to highly dynamic loads as a result of turbulent inflow and shear across the rotor plane.

Field test provided results that involve effects of both inflow anomalies and effects from operation in a 3-D environment. To separate these two effects and to solely understand the 3-D aerodynamic

effects on the wind turbine, a wind tunnel test was necessary. NREL please VI wind turbine was selected for this experiment. The turbine has two blades and a diameter of 10.058m. We will discuss the blade geometry in detail in Section 5.

Only wind tunnel that is big enough to fit a 10m diameter wind turbine is owned and operated by National Aeronautics and Space Agency (NASA) and is located at NASA Ames Research Center (ARC) at Moffett Field, California. The wind tunnel test section is 24.4m X 36.6m (80ft X120ft) [11]

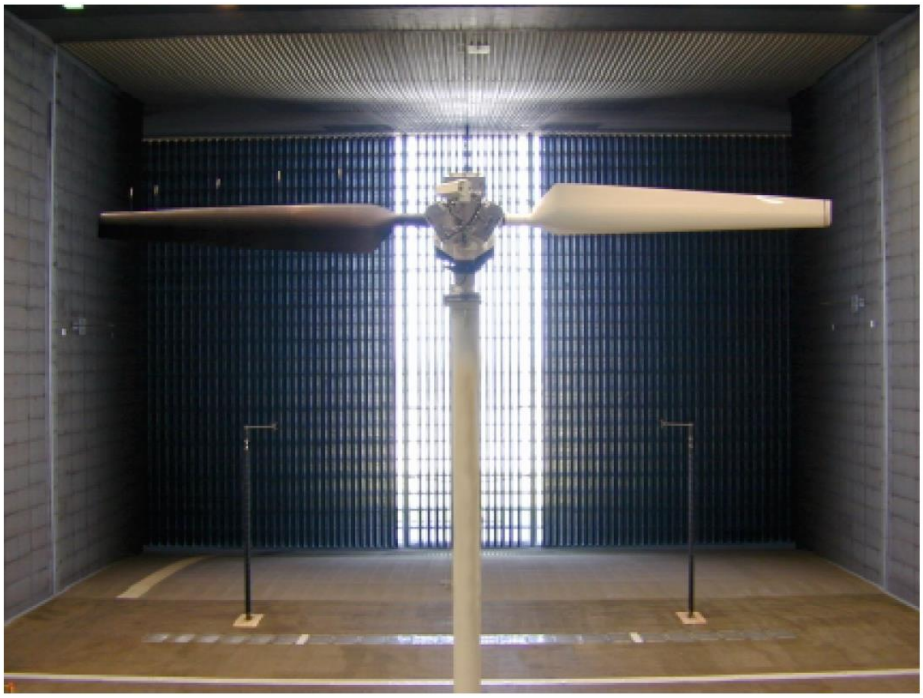

Figure 1 NREL Phase VI turbine experimental setup

[11]

The purpose of this experiment is to accurately acquire quantitative aerodynamic and structural measurement on a full-scale wind turbine free of inflow anomalies. The collected data will be used to validate and improve the performance of wind turbines and to design advanced wind energy machines. Key data collected include blade surface pressures, the angle of attack and inflow

dynamic pressure at five-span locations on one blade. Blade rotor bending moment and low-speed shaft torque are also calculated. After completion of the experiment, a science panel was called in and participants are encouraged to model the same wind turbine and the results from the numerical models were compared with the experimental results to validate the efficiency of numerical models. Due to this panel, there are many results that are available from numerical analysis and these results are helpful in validation and comparison in present work.

1.2. Wind energy and Wind Turbines

Humans have had the ability to harness wind energy for a long time now, with the earliest record of wind energy use dating back to 5000 B.C where wind energy is used to propel boats. Windmills came into popularity by early 200 B.C, where horizontal axis windmills where pumping water in China, and vertical axis windmills with woven reed sails where grinding grains in the Middle East.

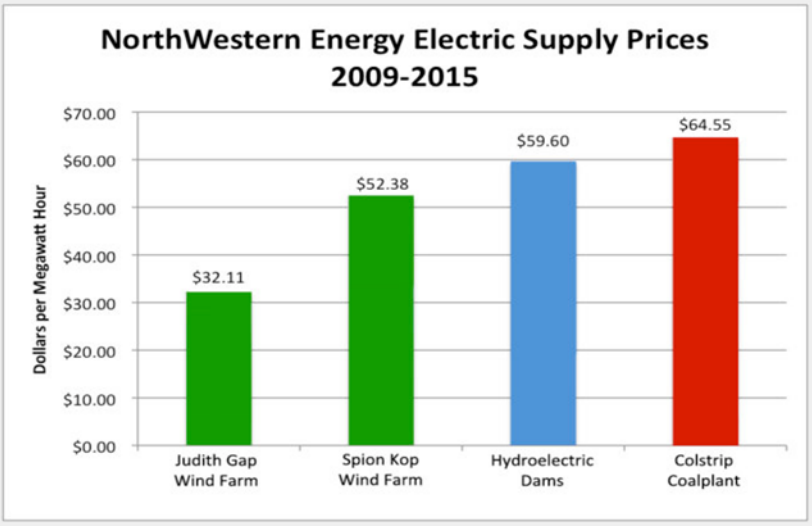

Figure 2 Source based cost of electricity, Northwestern Region

Over the course of time, and traveling merchants, carrying the idea of windmill across continents, windmills have served various purposes including grinding wheat & corn, pump water, cut wood at sawmills, draining lakes, and by end of 19th century Charles F. Bush realized the potential of

windmills in generating electricity for home and industrial purposes. Mr. Brush built the first electricity-generating wind turbine. The turbine has a diameter of 17m with 144 blades made of cedar wood and has a power output of 12kW.

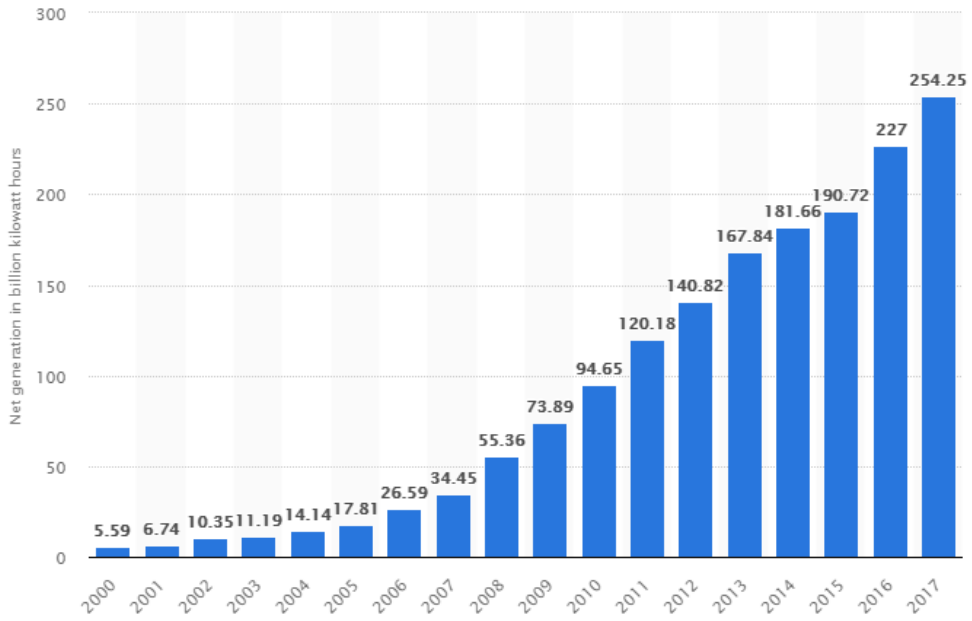

Figure 3 Wind energy production, 2000-2017

[12]

Wind turbines came in handy in electrifying rural areas of United States where electricity providing companies wouldn't reach mostly because of the costs involved. In the early 1990's wind turbines with a capacity of 5kW to 25kW where installed in remote areas. Since then wind turbines have become very popular in the United States and across Europe in Denmark and Germany, with the United States leading in the field. Wind turbines are widely used in World War I (up to 25kW capacity) and in World War II (Up to 200kW capacity) to power machinery both in the US and in Europe. With the oil crisis in 1973 US government heavily invested in Wind energy. With all the

incentives and tax exceptions the first breakthrough in wind energy was seen in California with the installation of a wind farm with a total energy capacity of 1.7GW.

Over the years leading to present day, with advancement in technology and wind energy becoming cheaper to produce, and global warming due to the use of fossil fuels, the world is shifting towards renewable energy. The Global Wind Energy Council (GWEC) said that global wind power capacity reached a total of 486.8Gw by end of 2016 and expected to reach 800GW by 2021. China, USA, and Germany are the top three countries leading the way in the installation of wind turbines and is responsible for a major share of wind energy produced across the world. Each of these countries has ambitious goals to increase the share of wind energy in total power generated for the future.

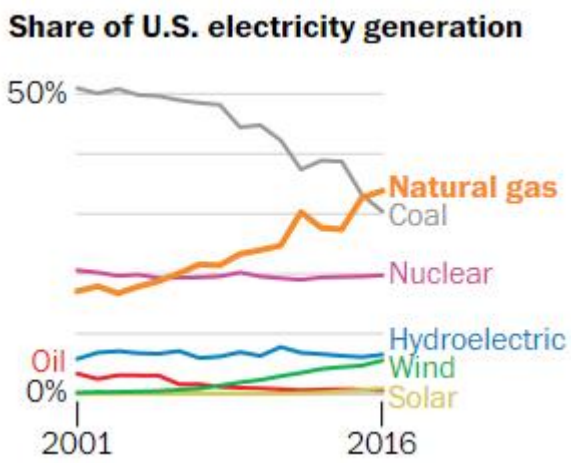

Figure 4 Source based power production trend *[33]*

In the United States, with nearly 29% of greenhouse gases coming from electricity sector it is important to use wind energy for electricity production, where wind energy produces 0.02 to 0.04 pounds of CO2/kWh compared to 1.4 to 3.6 pounds in coal and 0.6 to 1.2 pounds/kWh in natural gas-based power plants.

1.3. Wind Turbines

Wind turbines are broadly classified into two types

- Vertical Axis Wind Turbines (WAWT's)
- Horizontal Axis Wind Turbines (HWAT's)

1.3.1. Vertical Axis Wind Turbine

Vertical Axis Wind turbines commonly known as VWAT's has the main rotor shaft arranged vertically. The main advantage of VAWT is that it can generate power independent of wind direction, thus eliminating the need for pitch and yaw mechanisms and can be advantageous in areas with highly variable wind directions.

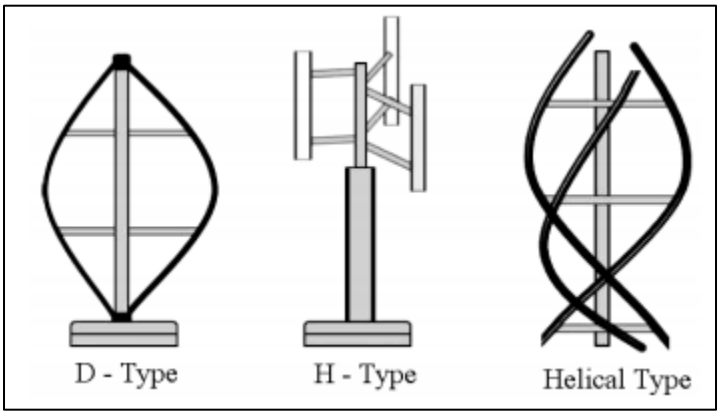

Figure 5 Types of VAWT rotors

[13]

Having a vertical axis, the turbines are generally installed on a base and generator and other components are placed on the ground which makes it easier for service and maintenance. VWAT are difficult to mount on a tower because of the high bending moment experienced by the tower

and hence cannot take advantage of higher wind speeds at high altitudes. For this reason, VAWT is ideal for building rooftops and high raised structures.

Although it is known to disturb the appearance of a building, it is very practical for the urban environment because of the easy installation process, low maintenance costs and low-risk operation. Because only one blade is producing lift at a time, VAWT's are inefficient compared to HWAT's. VAWT's also experience a problem of vibration as the airflow is turbulent. This vibration may result in a shorter lifetime for the bearings and causes sound pollution.

1.3.2. Horizontal Axis Wind turbine

Horizontal Axis Wind Turbines or HAWT's are the most common form of wind turbines with propeller-like looking blades that spin on a horizontal axis. Both the rotor shaft and the electric generator are mounted on the top of a tower. HAWT's requires the turbine to be pointed in the direction of the wind. In small wind turbines, this can be achieved using a simple wind vane placed square with the rotor blades. While larger turbines generally use a wind sensor coupled with a servo motor to turn the turbine in the wind direction.

Two most common installation configurations in HAWT's are upwind and downwind. In the upwind configuration, the turbine blades are placed upwind of the tower to avoid turbulence generated by the tower. The blades are designed to be stiff and placed a considerable distance ahead of the tower to avoid impact with the tower during high wind speeds. Although downwind configuration has more flexibility with the blade design and placement, the turbulence from tower leads to fatigue and affects the reliability of the turbine. Hence most of the HAWT's designed are upwind machines.

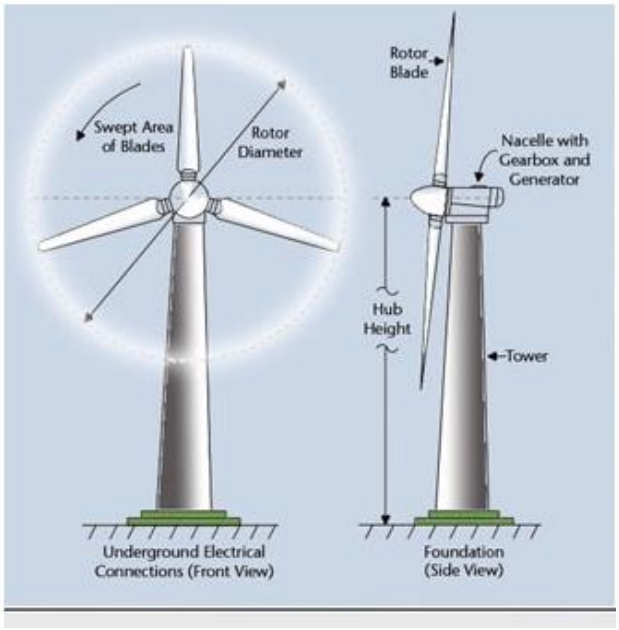

Figure 6 Wind turbine parts and terminology *[14]*

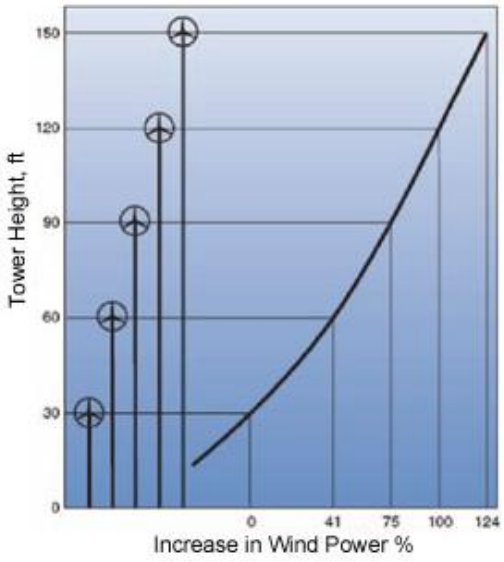

Figure 7 Increase in wind power as a function of tower height

Advantages of HAWT's also lie in the capability of the turbine to take advantage of higher wind speeds at high altitudes. Studies have shown that every ten meters up, the wind speed can increase by 20% and power output can increase by 34%. HAWT also take advantage of the fact that all the blades generate lift at a point of time compared to only one blade in VAWT making HAWT relatively efficient. Research in propeller design has also helped in optimizing the blade shape to achieve maximum aerodynamic efficiency. Along with the advantages, HAWT also have some disadvantages, with notable ones including lift and installation of components of the turbine, Requirement of additional equipment such as air velocity sensor, yaw and pitch control mechanisms. Overall the disadvantages outweigh the advantages in a HAWT and are a widely used form of wind turbine across the world.

The angular velocity of the turbine increases with an increase in wind speeds and at high speeds, the stresses and loads in the turbine far exceed the design limit. The rotor also has to rotate within a certain speed limit to generate constant power and limit fluctuations. Hence turbines are designed to control and limit the angular velocity. Rotor speed can be varied to control the output power but the power range which can be controlled by varying the rotor speed is very limited so that the changing the rotor speed can only be considered as a supplementary option. The most effective way to achieve controlled rotational speed and power is by controlling the angle of attack.

The most effective and proven ways to achieve controlled rotational speed and power are

- Pitch regulated turbines
- Stall regulated turbines

1.3.3. Pitch Regulated Turbine

The most effective way to influence the angle of attack is to adjust the rotor blade pitch. This can be achieved by turning the blade about its longitudinal axis using an electric or a hydraulic motor. Power input can be controlled by changing rotor pitch in two ways. It can either be adjusted to increase the power input or the angle of attack can be increased to a critical point to induce stall in the turbine blade and hence reduce the power intake. Pitch regulation is mostly used in larger wind turbines due to the need to accommodate the pitch regulating mechanism. At high wind speeds, blades are pitched in such a way that lift is decreased across the blade and drag is increased to slow down the turbine to a rated speed so that we can achieve a constant operational speed. Both pitch and stall regulated turbines behave the same way until the rated wind speed but pitch regulated turbine does a good job in maintaining constant power output throughout the rated wind speed till the cutoff speed. At cutoff speeds, where the rotation of the turbine can no longer be controlled by

blade pitch, the turbine is brought to a halt by applying breaks and the turbine no longer generates power.

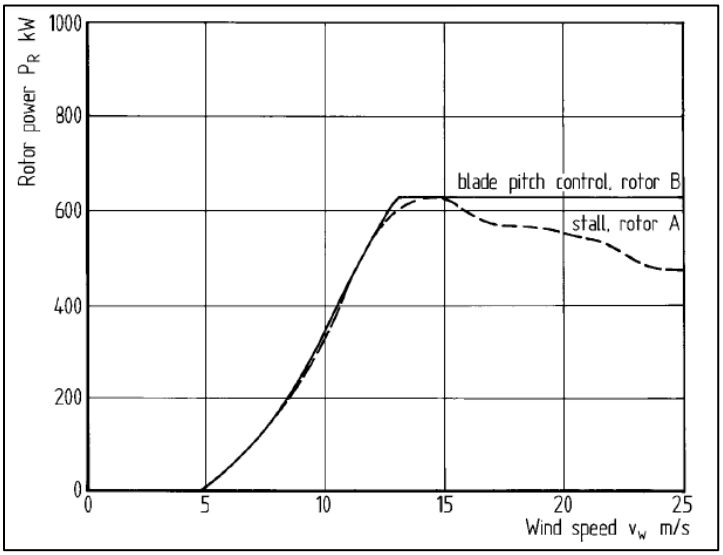

Figure 8 Rotor power generated by pitch regulated and stall regulated turbines

1.3.4. Stall Regulated Turbine

Unlike pitch regulated turbines where the blade is actively controlled, in stall regulated turbines we depend on the aerodynamic design of the blade to control the speed of the turbine and hence power production during high wind speed conditions. This is achieved by carefully varying the twist of the blade along the span. This approach eliminates the need for pitch control mechanisms and is optimal for small wind turbines and is generally applied in wind turbines with a rotor diameter of up to 20m. This approach also reduces total number of parts and hence less maintenance. But the strength and design of the blade in this configuration needs extra attention. Stall regulated turbines lag pitch regulated turbines in the rated wind speed region where the stall regulated turbine power output cannot be maintained constant but also decreases with an increase in wind speeds. Because the turbine does not have active blade controls, the blades might require

aerodynamic breaks in addition to mechanical rotor breaks to prevent runaway. The NREL Phase VI turbine we use in present work is a stall regulated upwind machine.

1.4. Biomimicry and Whale inspired wind turbines

Biomimicry is an approach to innovation that seeks sustainable solutions to human challenges by emulating nature's time-tested patterns and strategies. The core idea is that nature has already solved many of the problems we are grappling with. Animals, plants, and microbes are the consummate engineers. After billions of years of research and development, failures are fossils, and what surrounds us is the secret to survival. For example, when designing highspeed trains in Japan, engineers faced a challenge to minimize the tunnel boom and increase overall aerodynamics. The solution came from understanding the performance of a kingfisher bird. Inspired from the birds specialized beaks allowing them to dive into the water to hunt while making a minimal splash, trains that adopted this design where 10% faster and consume 15% less electricity than the previous models.

Another amazing find in biomimicry is the discovery of a harbor seals ability to identify vortices in the water and its ability to track the fish that created these vortices. More astonishing is the fact that they do not do this with their eyes but rather with their whiskers. Now researchers at MIT [15] are working on a model of harbor seal whiskers which will help in identifying the shape and size of the object ahead just by analyzing the wake from the object. This technology is further adapted to detect enemy submarines in water. Other examples include, paint inspired from whale skin used to reduce skin friction resistance on planes and boats,

Similarly, Humpbacks can maneuver their flippers to a sharp angle of attack before they start to stall, which lets them develop more lift and make those fish-catching turns. That's thanks to

tubercles, bumps that create scalloped edges on the leading side of their flippers. Professor Fish and his team engineered flippers with tubercles and without, and tested them in a wind tunnel at the Naval Academy. They found that the tubercles did delay stall, increasing the angle of attack up to 42%. This advantage is now being adapted to wind turbines to increase the power output. [1]

1.5. Wind Turbine Noise

Wind Turbine Noise mechanisms

Sound is always associated with rapid small-scale pressure fluctuations overlying the normal atmospheric pressure. These fluctuations are emitted from a source and travel as waves through the medium at speed of sound. These pressure fluctuations travel through medium and are perceived by the observer as a function of time and are referred to as sound pressure. Any unwanted and unpleasant sound is considered noise. Wind turbines are a constant source of noise and the sources can be mainly classified into

- Mechanical Noise
- Aerodynamic Noise

1.5.1. Mechanical Noise

Mechanical noise is caused by the relative moments of mechanical components and dynamic responses among them. Mechanical noises are mostly tonal in nature and can cause more annoyance even though the energy levels are smaller than aerodynamic sources.

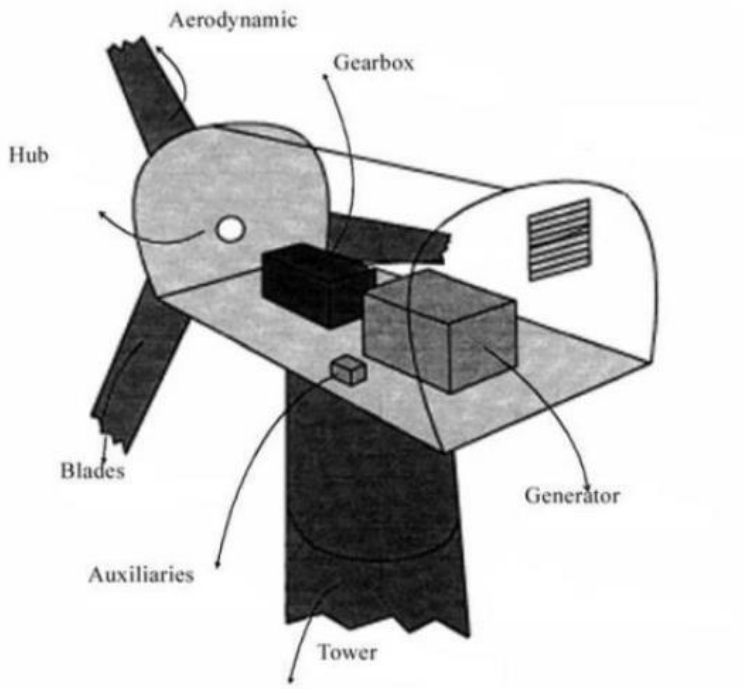

Figure 9 Sources of Mechanical Noise

[16]

Major contributors for the mechanical noise in a wind turbine are gearbox, generator, cooling fans, oil coolers, power packs for blade pitch, and the hub, rotor and the tower that act as loud-speakers transmitting and radiating the machinery noise. The noise is transmitted through two means namely airborne and structure-borne. As the name implies, airborne noise is directly transferred from the component to atmosphere whereas structure-borne is first transmitted from the source component to other structural components before transmitted into the atmosphere. Generator and auxiliaries can be considered as a source of airborne noise whereas tower and gearbox are some examples of components that are a source of structure-borne noise. Nacelle insulation and vibration isolation between machine parts and the enveloping nacelle could result in noise reduction. Few other noise reduction techniques include effective damping of noise transmission paths, splitting the nacelle casing and inclusion of flexible couplings.

1.5.2. Airfoil Self-noise

Trailing edge Noise

A boundary layer on a blade surface starts from the stagnation point on the leading edge, develops along the chordwise direction and transforms from laminar to turbulent. The transformation of the boundary layer from laminar to turbulent depends on factors such as Profile shape, the angle of attack, Reynolds number, the structure of surface and inflow disturbance. Important parameters describing the boundary layer turbulence are the length-scale of the energy-bearing turbulent eddies, the turbulent kinetic energy, its spectral decomposition, and the eddy convection velocity.

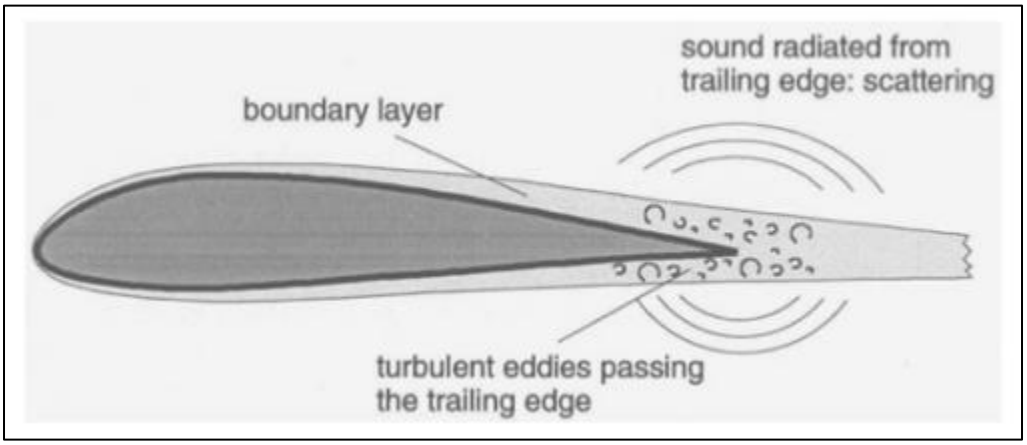

Figure 10 Trailing edge noise

[16]

At low Mach number, which is generally the case in the operation of wind turbines, turbulent eddies on a flat wall are inefficient noise sources, but the interaction of the turbulent eddies with Sharpe edges intensifies the noise and these noises become major sound sources. Hence, trailing edges of a turbine blade increase the efficiency of the noise radiation from the turbulent eddies in the boundary layer. This is the mechanism of turbulent boundary layer trailing edge interaction noise which is commonly referred to as trailing edge noise. Trailing edge noise peaks in the frequency range of 500-1500HZ depending on the type and operation of the wind turbine.

Laminar boundary layer vortex shedding noise

When a turbine operates in the Reynolds number range of 105 to 106 laminar region of the flow can extend up to the trailing edge of the airfoil. This boundary layer is likely to have instabilities and are known as Tollmein-Schlicting instabilities. These instabilities, when interacted with the trailing edge noise of same frequency, causes tonal noise. It is generated by a feedback loop between vortices being shed at the trailing edge and instabilities in the laminar boundary layer. High levels of noise occur when the instabilities are triggered by the acoustic field and vice versa. This laminar boundary vortex shedding noise is only significant in smaller wind turbines as most large turbines operate in a Reynolds number range of $3x10^6$.

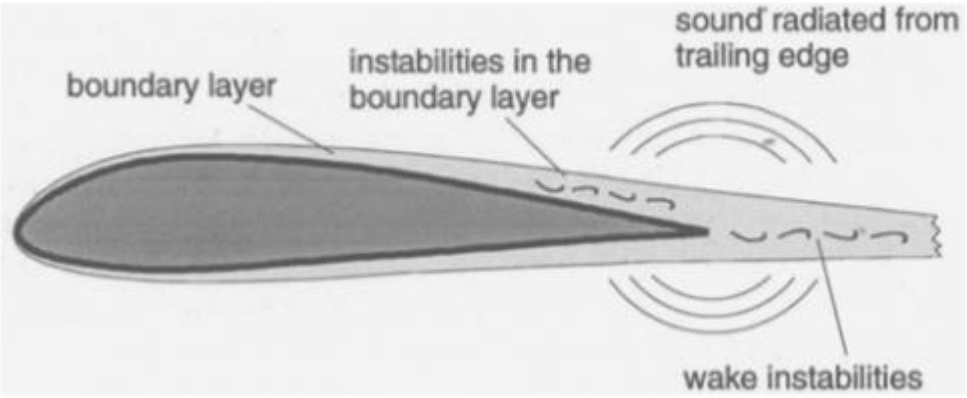

Figure 11 Laminar boundary layer vortex shedding noise

[16]

Tip Noise

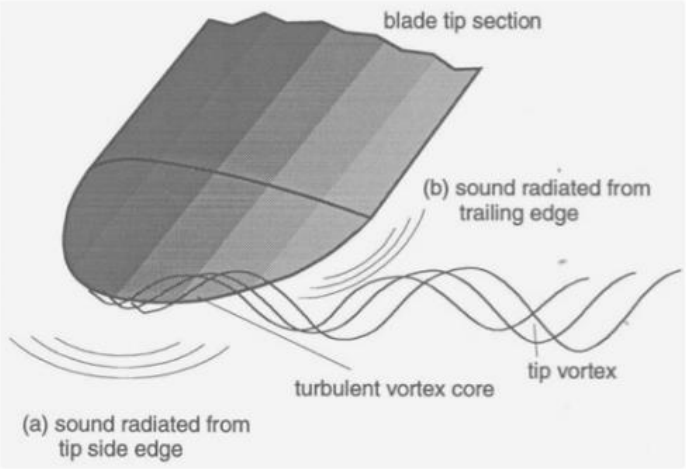

Figure 12 Tip Noise

[16]

The pressure difference between suction and pressure surface result in crossflow over the side of the blade tip which is responsible for the formation of tip vortex. Tip noise is believed to behave in the same way as trailing edge noise. Noise is generated because of the crossflow of flow over the side edge of the tip. Flow separation at side edge can also cause additional noise. Tip noise is mainly influenced by the convection speed of vortex and its spanwise extent and is characterized as broadband noise. The location of the vortex core, the strength of the vortex which depends on the angle of attack, Reynolds number and blade load distribution also have an influence on the intensity of the tip noise. The contribution to total noise by tip noise is generally small and in the order of 1-2 dB in some parts of the frequency range.

Separated/Stalled Flow Noise

A stall occurs when the angle of attack increases to a critical point where the flow is separated from the blade surface. This causes a substantial level of unsteady flow around the blade. A mildly separated flow causes noise radiation from the trailing edge whereas a deep stall flow causes radiation from the entire chord of the airfoil. A difference of 10dB increase is observed when trailing edge noise is compared with the stalled flow at low angles of attack. Noise callused by stalled flow is of broadband nature and is only major contributing noise mechanism beyond limiting angles of attack.

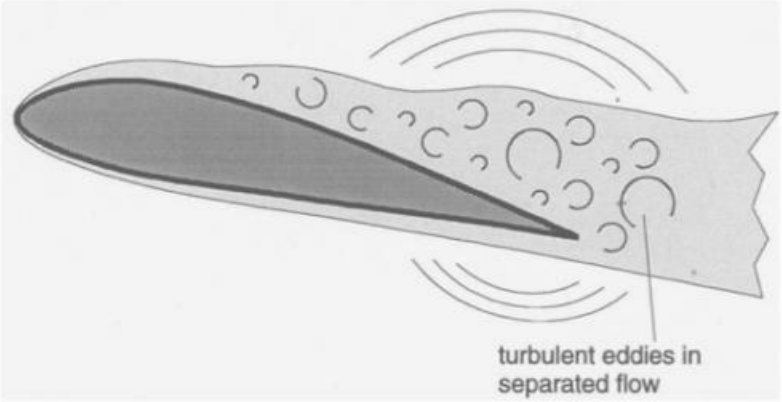

Figure 13 Stalled Flow Noise

[16]

Blunt Trailing Edge Noise

The blunt trailing edge noise depends on the trailing edge thickness and when the trailing edge reaches a critical thickness, alternating vortices produce surface pressure fluctuations in the near wake close to the trailing edge, which results in tonal noise. The trailing edge thickness and shape are the main characteristics defining the noise frequency. Sharpening the edge shifts the peak of the created frequency towards the ultrasound region. With the increase in the value of thickness, frequency, and bandwidth of tone decreases. For trailing-edge noise, the directivity and speed

dependence of the blunt trailing edge noise are considered equal. The geometry of the edge is a key factor in determining the generated noise amplitude. Compared to a rectangular shape, a round or a 60-90 degree wedge may double or triple the amplitude. A wedge angle smaller than 45 degrees or a bevel angle less than 60 degrees can give much lower amplitudes.

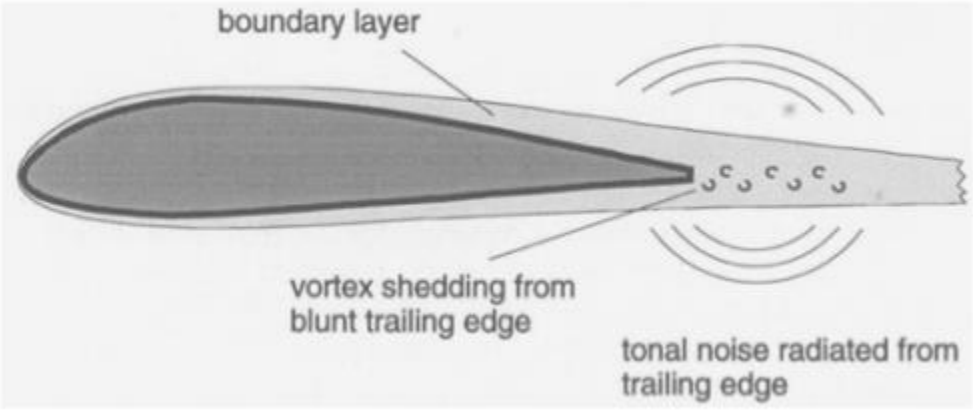

Figure 14 Blunt Trailing Edge Noise

[16]

2. Literature Review

Ece Sagol, Marcelo Reggio

Ece Sagol studied different two equation RANS turbulence methods to predict the wind turbine power and aerodynamic loads of an NREL phase VI rotor. The experiments are performed under the assumption of steady state, with a rotating reference frame and by keeping the blade stationary. To reduce computing costs, one blade is modeled instead of two and a rotational periodic boundary condition is applied.

Different turbulence models are tested and the model that best matches the experimental results of the NREL phase VI HAWT is chosen to perform further calculations. Predictions provided by SST k-w model are closest to experimental data at higher speeds and yields better estimate of the vortex shedding patterns of the flow.

Numerical analysis under-predicts LSST by 20% compared to the experimental results but yet exhibit the same pattern as UAE data. This poor compatibility is attributed to numerical methods low CFD prediction capability for widely separated flows. [17]

Masoud Ghasemian, Amir Nejat

Masoud Ghasemian, Amir Nejat focus on the Aeroacoustic analysis of NREL Phase VI wind turbine. Improved Delayed Detached Eddy simulation turbulence model is used to predict the turbulent flow field and Ffowcs Williams and Hawkings acoustic analogy is used to obtain far-field noise information. Masoud performed numerical analysis using IDDES for three different wind speeds and compared the results with SST K-Omega model and the experimental results. It is understood from the results that at high wind speeds and flow with large separations, IDDES method shows fewer discrepancies and more agreement with the experimental results compared

to RANS model and highlights the inability of RANS model to accurately predict the flows with massive separation. Acoustic results from IDDES model show good agreement with the experimental results. Thickness, loading noise, and quadrupole noise are calculated and the values suggest that quadrupole noise has a negligible effect on total noise and the Thickness and loading noise combination is the major source of the noise. It is understood that Sound pressure levels increase with an increase in wind speeds and the intensity of Overall sound pressure level (OASPL) observed by the receiver decreases with increase in distance from the turbine blade. [18]

A. Tadamasa, M. Zangeneh

This paper mainly deals with the prediction of Thickness and total noise and total noise using an impenetrable and permeable form of FW-H equations using results from SST K-Omega turbulent model based CFD solver. The paper evaluates the influence of variation in operation conditions on types of sound. It is observed that, with an operational tip Mach number of 0.12, loading noise is a dominant source of noise and quadrupole noise is insignificant at this speed compared to Loading and thickness noise. When the rotor speed is increased from 72RPM (M=0.12) to 210RPM (M=0.3), thickness noise becomes increasingly dominant and quadrupole noise become a significant noise source. With the unavailability of proper data to test FW-H models on wind turbines, the codes are validated using experimental results from other experiments like UH-1H helicopter rotor in hover and Hartzell aircraft propeller in forward motion. Once the FW-H models showed a good agreement with the experimental results in this case, FW-H model is then used to predict noise from NREL Phase VI wind turbine. [19]

Ri-Kui Zhang and Jie-Zhi Wu

Research by Zhang and Wu mainly focus on the aerodynamic characteristics of a wind turbine blade with a sinusoidal leading edge, inspired from flipper of a humpback whale, and the impact of leading edge dimensions on the power output. Reynolds-Averaged Navier-Stokes equation with the Spalart-Allmaras model is used for the numerical analysis by assuming the flow is fully turbulent. The author concludes that blade region from 60%R to the tip of the blade is highly important for the modified blade in improving the aerodynamic characteristics at high wind speeds. This improvement in performance is achieved by localized vortices shedding from the leading edge tubercles which can generate a higher peak of leading edge suction pressure than a regular blade.

The leading edge of NREL Phase VI is modified to mimic the whale flipper and wavelength and amplitude of the leading edge are varied in the range of $0.17c_o$ -$0.42c_o$ and $0.0125c_o$-$0.0375c_o$ respectively. The author observed five different configurations, by varying the values of wavelength and amplitude that root bending moment has no significant impact from the change in geometry and best torque can be generated at a wavelength of $0.25c_o$ and amplitude of $0.025c_o$. [5]

Giada Abate and Dimitri N. Mavris

The main aim of this research is to analyze the effect of improvement in aerodynamic characteristics of a wind turbine blade with a sinusoidal leading edge (Tubercles) on the power produced and the Annual Energy production (AEP). Amplitude (A) and wavelength (λ) of the tubercles are considered as the design parameters. Using Design of Experiments (DoE), 20 test cases are generated with an amplitude range of $0.01c_o$-$0.05c_o$ and a wavelength range of 0.016R-0.075R. Where c and R are chord and span of the NREL Phase VI blade respectively. Considering

the flow to be steady, Incompressible and fully turbulent, CFD analysis was performed in STAR CCM+, using RANS equations and SST K-Omega model. The author came to the same conclusion as Zhang and Wu that the modified blade performs better than a standard blade at higher wind speeds of 15-25m/s. Annual Energy Production is calculated using the formula,

AEP = $\overline{P}$.365.24 , Where $\overline{P}$ is the average power produced by the wind turbine.

Average power is calculated based on the probability distribution of wind speeds. In this work, it is calculated using Rayleigh probability distribution. It is observed from the results that, though all the modified blade cases perform better at higher wind speed conditions, only some cases show improvement in AEP. And noticed is the fact that cases with improved AEP have a higher value of wavelength. [6]

Majid Asli, Behnam Mashhadi Gholamali, and Abolghasem Mesgarpour Tousi

This research mainly deals with the lift, drag and flow separation properties of the modified blade with tubercles compared to a baseline S809 airfoil. A three-dimensional infinite blade numerical analysis is performed on the baseline and the blade with a sinusoidal leading edge. The wavelength of the modified LE is 25% of chord and the amplitude is 2.5%. These values are specifically chosen to mimic the geometry of the humpback whale flipper. It is observed from this study that, a stall occurs in the baseline airfoil at around 17 degrees of Angle of Attack (AoA) with a sudden drop in lift coefficient, stall in the modified airfoil occurs comparatively early with a smooth reduction in lift coefficient. On the other hand, a modified airfoil always have a higher drag coefficient because of the presence of larger layer separation territory than the baseline. The explanation behind the difference in the aerodynamic behavior of both airfoils is that, though the flow is attached at AoA=5 degrees on both the airfoils, at higher AoA, when the flow starts to separate on

the baseline airfoil, on the modified airfoil the flow diverges from peak of the bump and form swirl vortex in through area. These generated vortices become bigger with an increase in angle of attack. These high energy vortices can delay the flow separation over the airfoil by reenergizing and adding momentum to the boundary layer flow over the airfoil. This keeps the boundary layer attached to the surface and prevents large separation and a sharp decrease in lift coefficient. [20]

Milosevic, D.S.; Murray, M.M. ; Howle, L. E.; Fish, F. E.

This research [2] is one of the earliest works on the effect of leading edge tubercles on stall delay, inspired by humpback whale's ability to undertake acrobatic underwater maneuvers to catch prey. The author concludes that leading edge tubercles can delay the stall angle by approximately 40% while increasing lift and reducing drag. Experiments were performed on two scale models of the flipper, one with and one without tubercles and Coefficient of Lift and Drag with an angle of attack range of -2 to 20 degrees are calculated. For the smooth flipper, stall occurs at 12 degrees with a 13% decrease in lift coefficient and a subsequent decrease from 0.78 to 0.38 with an increase in angle of attack from 12.1 to 18.5 degrees. Comparing smooth flipper with the one with tubercles, the slope is similar to that of the smooth flipper, but stall angle increases by 40% to 16.3 degrees with a 6% increase in maximum coefficient of lift. The coefficient of Drag curve for both the models show similar pattern till the angle of attack of 12degrees. Beyond this, the model with tubercles produces as much as 32% less drag than the smooth model. The superiority of the model with tubercles is also proven in the values of lift to drag ratio where the model with tubercles have a higher value of lift to drag ratio at higher angles of attack. This availability of higher lift with reduced drag helps humpback whale to maneuver at a high angle of attacks. [2]

3. Mesh Setup

Mesh is the critical part of a numerical analysis for an accurate solution and Mesh setup can have a greater impact on time and computational expenses. Hence choices for mesh are carefully considered to minimize computational costs with a negligible compromise in accuracy.

3.1. Mesh Models

3.1.1. Polyhedral mesh:

Many commercial software tools as a standard practice use tetrahedral volume mesh for its simplest volume elements and ease of auto-generation. But when using tetrahedral mesh in large domains larger number of control volumes are needed since tetrahedra cannot be stretched too much. Also, tetrahedral control volumes have only four neighbors and cannot be accurate in the analysis. Special discretization techniques and a large number of cells are needed to achieve accurate solutions and good convergence in tetrahedral meshes.

To overcome this disadvantage, the polyhedral mesh is used, which provides the same benefits as of tetrahedral mesh and avoid the short comes.

A polyhedral cell has many neighbors (in the order of 10), hence gradients can be much better approximated than tetrahedral. A polyhedral mesh can be efficient at corners and along walls where cells have a couple of neighbors, thus having the ability to predict the gradients and local flow distribution. Also, the polyhedral mesh is less sensitive to stretching than tetrahedral mesh and smart grid generation and optimization techniques help in improvement in grid quality which improves solver efficiency and solution accuracy.

A polyhedral cell with 12 faces, 6 optimal flow directions and with a larger number of neighbors can provide more accurate results with a smaller number of cells when compared to tetrahedral cells with three optimal flow directions. Many comparisons verified that with polyhedral mesh,

one needs four times fewer cells, half the memory and tenth to a fifth of computing time compared to tetrahedral meshes to reach the same accuracy. Polyhedral is also efficient in conformal meshing, which will be useful in the present case to generate periodic boundary [21].

3.1.2. Wall treatment

It is important to accurately resolve the flow and turbulence properties of a boundary layer since walls are a source of vorticity inflow problems of practical importance. To properly mesh the boundary layer, it is essential to understand the inner regions of the boundary layer.

A boundary layer is divided into three layers based on the flow characteristics and is model using different approaches. A non-dimensional wall y^+ value is used to define the stretching of the sublayers. The viscous sublayer is the layer closet to the wall and is dominated by viscous effects and the flow is almost laminar ($y^+ \leq 5$). Viscous and turbulence effects are equally dominant in a Log-law layer ($30 < y^+ < 500$) and a Buffer layer is a transition layer from viscous sublayer to Log-law layer ($5 < y^+ < 30$). A non-dimensional wall y^+ value is used to define the stretching of the sublayers. [22]

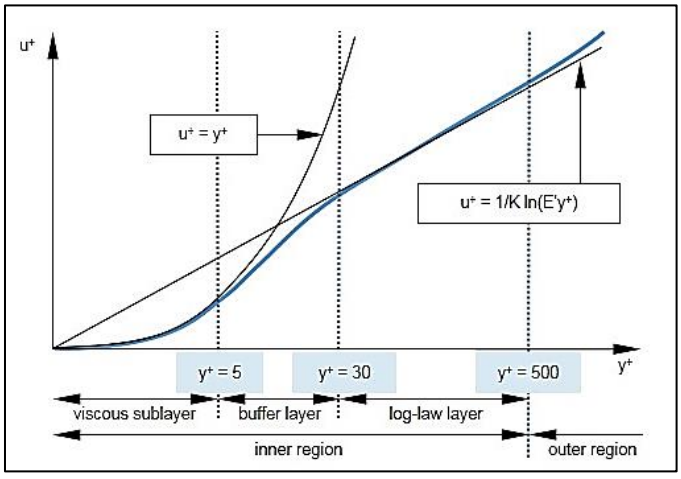

Figure 15 y+ Vs Dimensionless velocity

Star CCM+ offers three type of wall treatment, a low-y^+ wall treatment, which resolves the viscous sublayer but requires a considerably fine mesh and can add to the computational cost. A high-y^+ wall treatment reduces the number of near wall cells, with a near to wall cell located in the Log-law layer at a $y^+>30$. This wall treatment does not resolve the viscous sublayer but derives shear stress and turbulent dissipation from equilibrium turbulent boundary layer theory. In the current case, for accurate prediction of pressure drop, flow separation and drag the viscous sublayer should be completely resolved and hence a $y^+\sim 1$ is targeted. The all y^+ wall treatment model is chosen for the present work. [22]

3.1.3. Prism Layer Mesher

A prism layer mesh is important to properly capture the thin and complex boundary layer physics. Prism layer mesher eliminate the need to use fine mesh throughout to capture the boundary layer, which can be computationally expensive. Use of the prism layer near the wall is cost effective and time-saving. Prism layer can accommodate high aspect ratio cells without incurring an excessive streamwise resolution.

Prism layer mesher offers three distribution modes which include, Stretch Factor, Wall thickness and thickness factor. Wall thickness mode, which allows the user to define the first cell layer thickness or the distance from the wall to the first cell center is selected in the current work to ensure wall y^+ value is in the desired range. Other important factors in the prism layer meshing include stretching factor, which defines the ratio of one prism layer to the next. Stretching factor of a prism layer needs to be in the range of 1.1~1.5 where a smaller stretching ratio leads to the insufficient growth of prism layer and leads to a higher aspect ratio between the top layer of the prism mesh and the bulk mesh which can reduce the accuracy of the solution. A larger stretching ratio can hinder the ability of prism mesh to resolve the boundary layer completely. Though the

number of prism layers does not have much impact on accuracy, it helps to use an optimal number of prism layer as required by the model to limit the number of cells and to improve the convergence time.

3.2. Mesh parameters

3.2.1. Prism layer mesher

Keeping in mind the interest of completely resolving viscous sublayer, the value of wall y^+ is maintained below 1 for most of the blade surface and was not allowed to exceed a value of 5. This is achieved using wall thickness model. Prism meshing at the leading edge and trailing edge proved to be challenging around the edges. A layer reduction percentage property of STAR CCM+ which helps reduce the number of prism layers as the thickness of the prism layer decreases to maintain low aspect ratio, better mesh quality and reduce skewness angle error in the cells.

Parameter	Value
Stretching Function	Geometric Progression
Distribution Mode	Wall Thickness
Near Wall Thickness	1.0^{-5}m
Expansion Ratio	1.2
Prism Layer Thickness	0.01m
Layer Reduction Percentage	50%
Gap Fill Percentage	25%
Minimum Thickness Percentage	10%

Table 1 Prism layer parameters

3.2.2. Surface Mesher

A high-quality surface mesh is necessary to generate a volume mesh and prism mesh in a numerical analysis. To achieve this requirement STAR CCM+ offers a Surface remesher to model and configure surface mesh. Surface remesher improves the overall quality of an existing surface by retriangulating to make the surface optimal for volume meshing and it also aids the subsurface generator in the prism meshing process.

Surface mesher also include an option for localized refinement for part surfaces, boundaries and curves. This option is extremely useful when meshing the Leading edge and Trailing edge of the wind turbine blades where the surface area is small and curved. By refining the LE & TE, generation of prism layers at these edges is made possible without any bad cells.

Surface or Curve	Cell Size
Blade surface (Relative min., Target Size)	0.0025m, 0.01m
Leading edge Curve (Relative min., Target Size)	0.001m, 0.001m
Trailing edge Curve (Relative min., Target Size)	0.001m, 0.001m
Blade tip (Relative min., Target Size)	0.001m, 0.0015m

Table 2 Surface Mesh properties

3.2.3. Polyhedral Mesh & Volumetric controls

An unstructured polyhedral mesh is opted for the volume mesh in the domain. A stretching factor is used to control the growth rate of the volume mesh to maintain acceptable volume change ratio.

Parameter	Value
Base Size	0.01m
Surface growth rate	1.2
Inlet (Relative min., Target Size)	0.5m, 2m
Outlet (Relative min., Target Size)	0.5m, 2m
Domain Slip surface (Relative min., Target Size)	0.5m, 2m
Periodic Surface, 1&2(Relative min., Target Size)	0.5m, 2m

Table 3 Volume Mesh Properties

The size of the mesh around the wind turbine blade and the mesh leading to the FW-H receiver should be very fine in order to capture the flow and the acoustic pressure accurately. Considering the size of the domain it is difficult to achieve the required only with the use of volume meshing which will result in huge cell count and in turn very computationally expensive. For this very reason STAR CCM+ offers volumetric controls to limit the use of fine mesh only in the areas required and in the required shape.

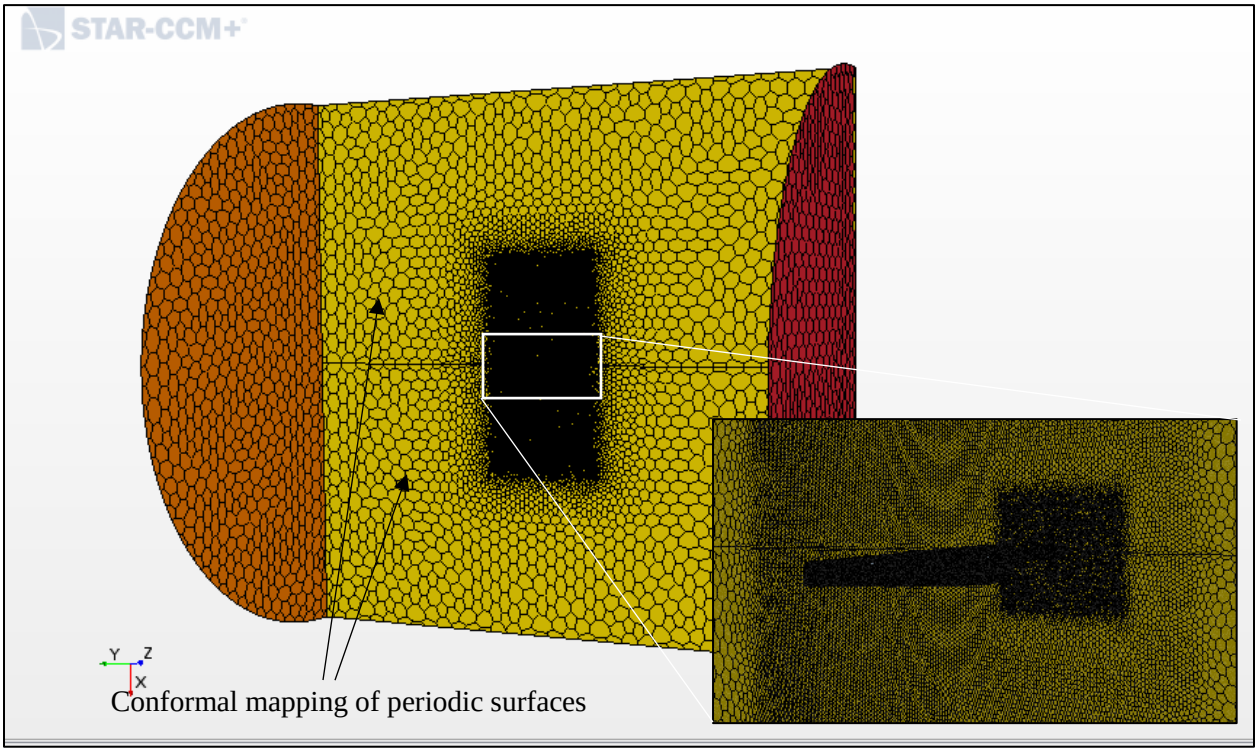

Figure 16 Polyhedral Volume mesh

A volumetric control in the shape of a block is created immediately around the blade to accurately capture the flow physics around the blade such as flow separation on suction surface and vortex generation. A cylindrical volume control which includes the area of complete blade rotation and FW-H receiver is used to capture the sound pressure variation generated by the blade.

Parameter	Value
Cell size, Block	**0.04m**
Cell Size, Cylinder	**0.2m**

Table 4 Volumetric control cell dimensions

3.3. Mesh Quality

Quality of the generated mesh heavily affects the accuracy of the solution and the efficiency of the solver. For these reasons, it is important to make sure that the mesh is free of any bad cells. Of various metrics for which a cell can be categorized as bad, we will discuss the ones that we encounter in current research.

Volume change parameter can be defined as the ratio of the volume of the cell to that of its largest neighbor. A ratio of 1 means cell has equal to or higher volume than its neighbor. A higher volume change among neighboring cells can result in potential inaccuracies in the solution and hence not desirable. Similarly, cells with good skewness permit the diffusion of quantities without them becoming unbounded. Skewness angle is the angle between the face area vector and the vector connecting the two centroids. Good skewness angle is essential to eliminate any solver convergence issues. Since the dimensions of the blade trailing edge is small compared to the rest of the geometry, it is possible to encounter chevron cells at this location. Chevron cells are pairs of thin slender cells which meet at a common face at an angle such that line joining the cell centers does not pass through the common face. Cells are quantified as 1.0 or 0.0 using chevron quality norm. 1 being chevron cells and 0 being regular cells.

Chevron quality norm, $c = 1 - \frac{dp.dp}{\max(dp.dv)}$ (1)

Where,

dp is a vector projected from the face center to the line joining the cell centers.

dv is the vector from the face vertex to the face center.

And the max function, in evaluating the chevron quality norm, is taken over all the face vertices.

STAR CCM+ provides a tool to isolate and remove any bad or undesired cells based on above-mentioned metrics and at desired threshold values. Table *5* below provides the thresholds used for various metrics.

Cell quality parameter	Threshold value
Face Validity	< 1.0
Cell Quality	<1.0E-8
Volume Change	<0.01
Contiguous Cells	<100000
Volume	<0 m^3
Skewness Angle	>85
Chevron Cells	<1

Table 5 Mesh quality threshold parameters

Once the undesired cells are isolated, measures are taken to eliminate these cells. These measures include localized refinement of mesh and improving the smoothness of geometry.

3.3.1. Mesh Independence analysis

To evaluate the independence of the solution from the mesh setup, a mesh independence analysis is performed. Cell base size of the mesh is varied, and all other parameters are defined as a function of cell base size. This analysis helps us in choosing an optimal mesh which provides accurate results without compromising computational costs. 6 different grid sizes are tested, and it can be observed that a grid with 5.3mil cells provides the most accurate results with less computational cost. But to accurately capture the flow around the blade a fine volumetric control around the blade is necessary and thickness of the prism layer, which is a function of cell base size must be fine enough to capture the boundary layer flow. The mesh is further resolved in these two areas for accurate flow prediction and mesh with a base size of 0.01m and cell count of 8.8 million is selected for the baseline blade. A similar method is followed for the modified blade and the final mesh has a base size of 0.01m and total cell count of 9.39 million.

Cell size(m),	Number of cells (Million)	Torque, Nm
0.025	2.37	610.02
0.02	3.177	634
0.017	3.93	645.72
0.014	5.28	652.34
0.01	8.8	654.23
0.009	10.72	656.44

Table 6 Mesh Independent Study

4. Physics

In the current research, a commercial CFD software, STAR-CCM+ is used for numerical analysis. Though the flow is unsteady at and above speeds of 15 m/s initial numerical analysis of baseline blade and sinusoidal leading-edge blade are performed using Steady Reynolds Averaged Navier-Stokes (RANS) equations with the segregated Menter's SST k-ω turbulent model and all y^+ wall treatment.

4.1. Reynolds–Averaged Navier–Stokes Equations

RANS turbulence models provide closure relations for the Reynolds –Averaged Navier -Stokes equations that govern the transport of the mean flow quantities.

To obtain the Reynolds-Averaged Navier-Stokes equations, each solution variable ϕ in the instantaneous Navier-Stokes equations is decomposed into its mean, or averaged, value $\bar{\phi}$ and its fluctuating component ϕ'.

$$\phi = \bar{\phi} + \phi'$$

Where ϕ represents velocity components, pressure, energy, or species concentration

The averaging process may be thought of as time-averaging for steady-state situations and ensemble averaging for repeatable transient situations. Inserting the decomposed solution variables into the Navier-Stokes equations results in equations for the mean quantities.

The mean mass and momentum transport equations can be written as:

$$\frac{\partial \rho}{\partial t} + \nabla.(\rho \bar{v}) = 0 \tag{2}$$

$$\frac{\partial}{\partial t}(\rho \bar{v}) + \nabla.(\rho \bar{v} \otimes \bar{v}) = -\nabla.\bar{p}I + \nabla.(T + T_t) + f_b \tag{3}$$

Where,

- ρ is density
- $\bar{v}$ and $\bar{p}$ are mean velocity and pressure respectively.
- I is the identity sensor.
- T is the viscous stress tensor.
- F_b is the result of the body forces.

The averaging process, which is similar to the time-averaged steady-state situation, yields equations for mean quantities that are identical to the actual equations but add a tensor quantity to momentum transport equation, known as Reynolds stress tensor.

Reynolds stress tensor can be defined as

$$T_t = -\rho \begin{pmatrix} \overline{u'u'} & \overline{u'v'} & \overline{u'w'} \\ \overline{u'v'} & \overline{v'v'} & \overline{v'w'} \\ \overline{u'w'} & \overline{v'w'} & \overline{w'w'} \end{pmatrix} \tag{4}$$

Where:

- ρ is the density.
- u, v and w are the velocity components.

To model T_t in terms of mean flow quantities, STAR CCM+ offers two basic approaches to provide closure for the governing equations,

1. Eddy Viscosity model
2. Reynolds Stress transportation model (RST)

Considering the limited resources, Eddy Viscosity models are focused over RST models, where one need to solve seven equations instead of two in some of Eddy Viscosity models. Along with the obvious cost of computational time to solve the seven equations, the solution can also require more iterations to converge owing to the numerical stiffness of RST equations.

Among Eddy viscosity models, Spalart-Allmaras model is a one equation model that solves the transport equation for modified diffusivity, $\bar{\nu}$ to determine the turbulent eddy viscosity. The main application of Spalart-Allmaras is in the flows where there is very limited or no separation of flow and is suitable for flows over wing or fuselage and is not suitable for the current study of a wind turbine, which involves flow separation.

K-Epsilon model is a two-equation model which solves the transport equation for turbulent kinetic energy, k and turbulent dissipation rate ε. K-Epsilon model is among the most widely used models since its inception. It provides a good balance between robustness, computational cost, and accuracy. Like the K-Epsilon model, K-Omega is a similar two-equation model that solves turbulent kinetic energy and specific dissipκation rate ω to determine the turbulent eddy viscosity.

Though the two models sound similar, K-Omega is superior to K-Epsilon in its improved boundary layer performance under adverse pressure gradient and that it can be applied to boundary layer including viscous dominated region without further modification, but is extremely sensitive to inlet boundary conditions for internal flows, unlike K-Epsilon model.

4.2. SST K-Omega model

SST K-Omega model is a blend of K-Omega and K-Epsilon models, to take advantage of robustness of K-Omega in near-wall region and free stream independence of K-epsilon in the far field [23]. SST K-Omega model was proposed by Mentor who developed a method to transform epsilon from the K-Epsilon model to an omega transport equation by variable substitution. The transformation adds an additional diffusion term $\nabla k.\nabla \omega$ to the original K-Omega model.

$$\frac{\partial}{\partial t}(\rho k)+\frac{\partial}{\partial x_i}(\rho k u_i)=\frac{\partial}{\partial x_i}\left(\Gamma_k \frac{\partial k}{\partial x_j}\right)+G_k-Y_k+S_k \tag{5}$$

$$\frac{\partial}{\partial t}(\rho k)+\frac{\partial}{\partial x_i}(\rho k u_i)=\frac{\partial}{\partial x_j}\left(\Gamma_\omega \frac{\partial \omega}{\partial x_j}\right)+G_\omega-Y_\omega+D_\omega+S_\omega \tag{6}$$

Where

G_k represents the generation of turbulent kinetic energy attributed to mean velocity gradients,

G_ω represents the generation of ω

Γ_k and Γ_ω represents the effective diffusivity of k and ω respectively.

Y_k and Y_ω represent the dissipation of k and ω attributed to turbulence.

S_k and S_ω are user-defined source terms.

And, D_ω represents the cross-diffusion term.

Mentor suggests that by using a blending function, a function of wall distance. A blending function is used to control the application of cross diffusion term. Using the blending function, we can

include the cross-diffusion term far from walls, but not near walls, effectively blending the K-epsilon model in the far field with K-Omega model near wall [24].

SST κ-ω model is selected for current work as its found to be more accurate than other turbulent models [25] and is computationally less expensive [17] [18].

4.3. Curle Broadband Noise source model

Curle model represents dipole noise from turbulent boundary layer flow over a solid body at low Mach number. Dipole noise represents the noise from the surface pressure fluctuations, a result of the interaction of solid boundaries with fluids. Curle model calculates the local contribution of acoustic power per unit area of the body surface.

The Curle model is highly compatible with model choices in the current research. Curle noise source model is suitable with steady-state Reynolds-Averaged Navier-Stokes turbulent equations and is available for segregated and coupled flows.

The acoustic pressure can be written in terms of the local contributions as;

$$\rho' = \frac{1}{\left(4\pi a_o^3\right)} \int_S \left[\frac{\left(x-y\right)}{r^2} \frac{\delta p}{\delta t}\left(y, t - \frac{r}{a_o} \right) \right] . n dS(y) \tag{7}$$

Where:

ρ' is the acoustic pressure

a_o is the far-field sound speed

$t-r/a_o$ is the emission time

p is the surface pressure

x is the position in the far-field

y is the point in the far-field where the noise is calculated, measured a face centroid on the solid boundary mesh.

r is |x-y|

n is the wall-normal direction

Surface Acoustic Power, the measure of local contribution to acoustic power per unit surface area can be calculated from

$$SAP = \int_S I(y) dS(y) \tag{8}$$

Where I(y) is the directional acoustic intensity per unit surface.

And surface acoustic power can be represented in dB using,

$$SAP(dB) = 10 \log \frac{SAP}{P_{ref}} \tag{9}$$

Where P_{ref} is the reference acoustic pressure.

5. Blade Geometry

In current work, two wind turbine blade performances are compared. One is an original NREL Phase VI wind turbine, and the other blade is a phase VI turbine with a modified leading edge. We will discuss the geometry of both the model in this section.

5.1. NREL Phase VI Blade

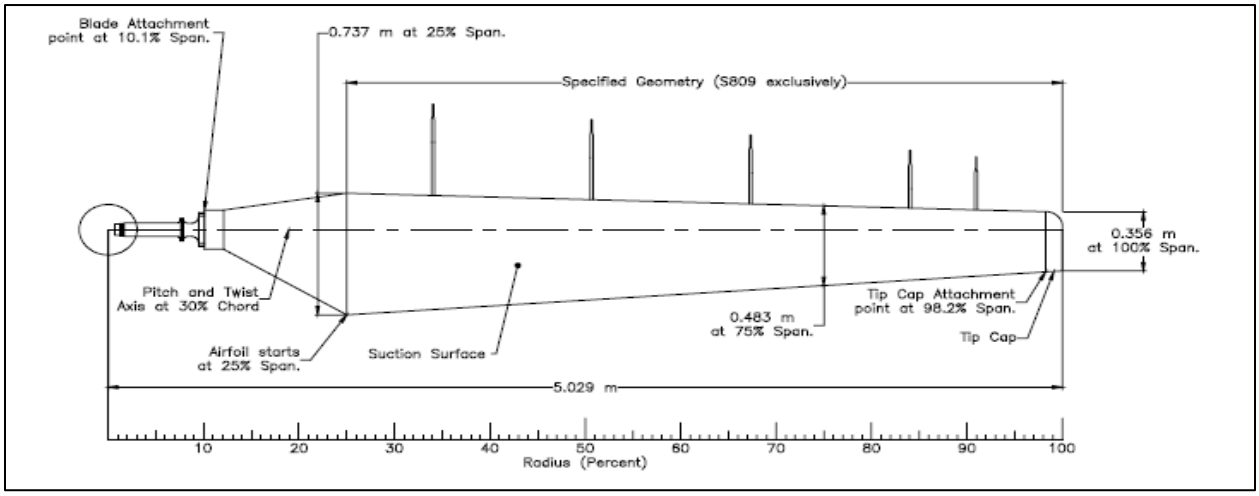

Figure 17 NREL Phase VI Wind turbine Blade

The phase VI rotor is a stall-regulated rotor designed by Giguère and Selig under contract by NREL from March1998 through March1999 [26]. The original NREL Phase VI is a stall regulated wind turbine with a rated power output of 19.8kW. The turbine has a diameter of 10.058m with a rotational speed of 72RPM and has two blades. Each turbine's span of 5.029m is divided into three sections, a cylindrical section, a transition region, and the S809 airfoil section. The hub radius of the turbine is 0.508m. The cylindrical section starts from the hub and extends to 0.883m and the airfoil section starts from 25% of the span. A transition region connects the airfoil region to the cylindrical region from 0.883m to 1.257m. S809 is a thick airfoil, widely used in wind turbines for

its efficiency. The airfoil blade section is linearly tapered with a maximum chord length of 0.737m at 25% span and twisted nonlinearly such that the blade tip pitch is 3 degrees.

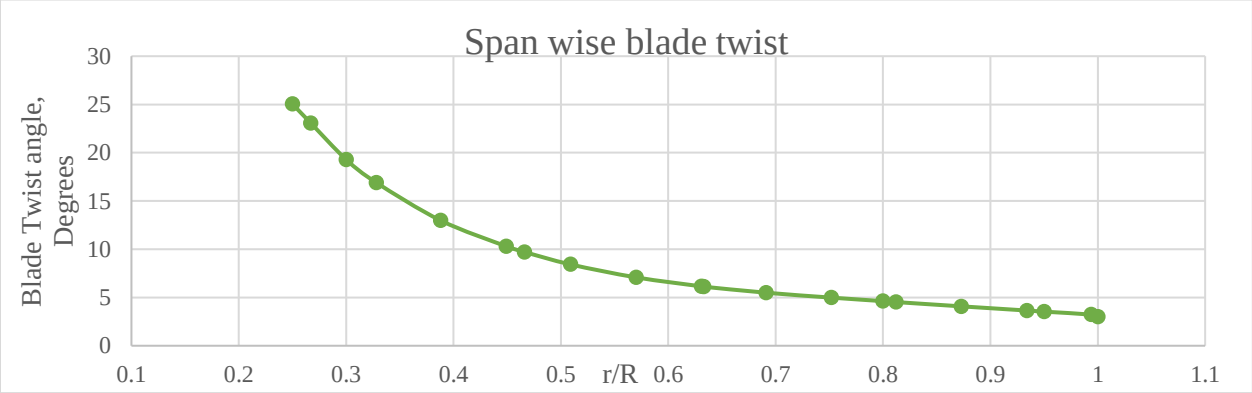

Figure 18 Spanwise blade twist distribution

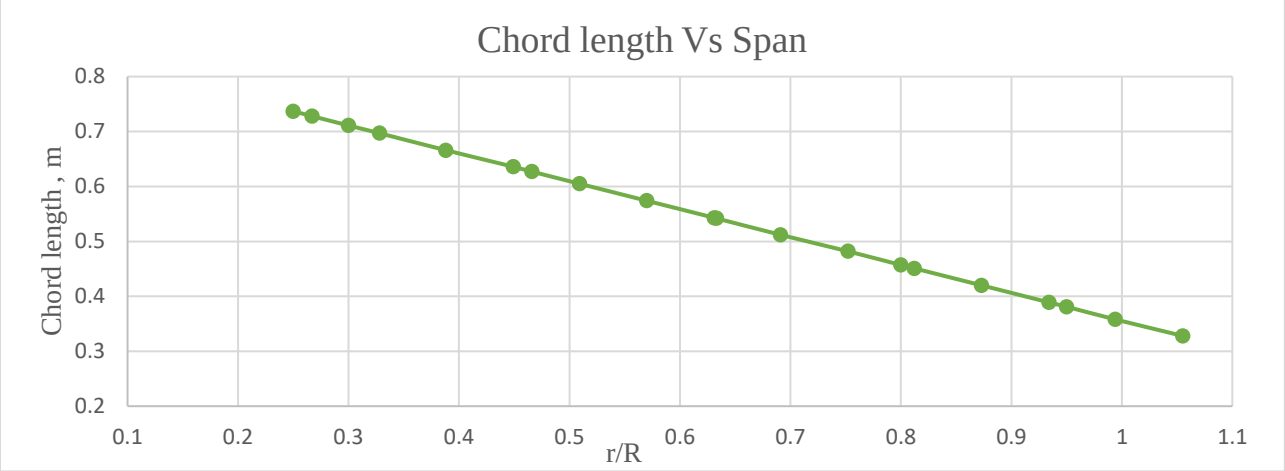

Figure 19 Spanwise blade chord length

The trailing edge of the S809 airfoil section has been trimmed from sharp trailing edge to blunt trailing edge by reducing 2% of the chord length. The trailing edge is changed to a curve sharp to accommodate prism layers and also, a sharp trailing edge adds to the structural instability of a blade and hence requires bluntness. The trimmed trailing edge is converted into a semicircle and points for the circle are generated using circle equation. CAD for the blade is performed on SRAR CCM+ using tools like extrude and loft.

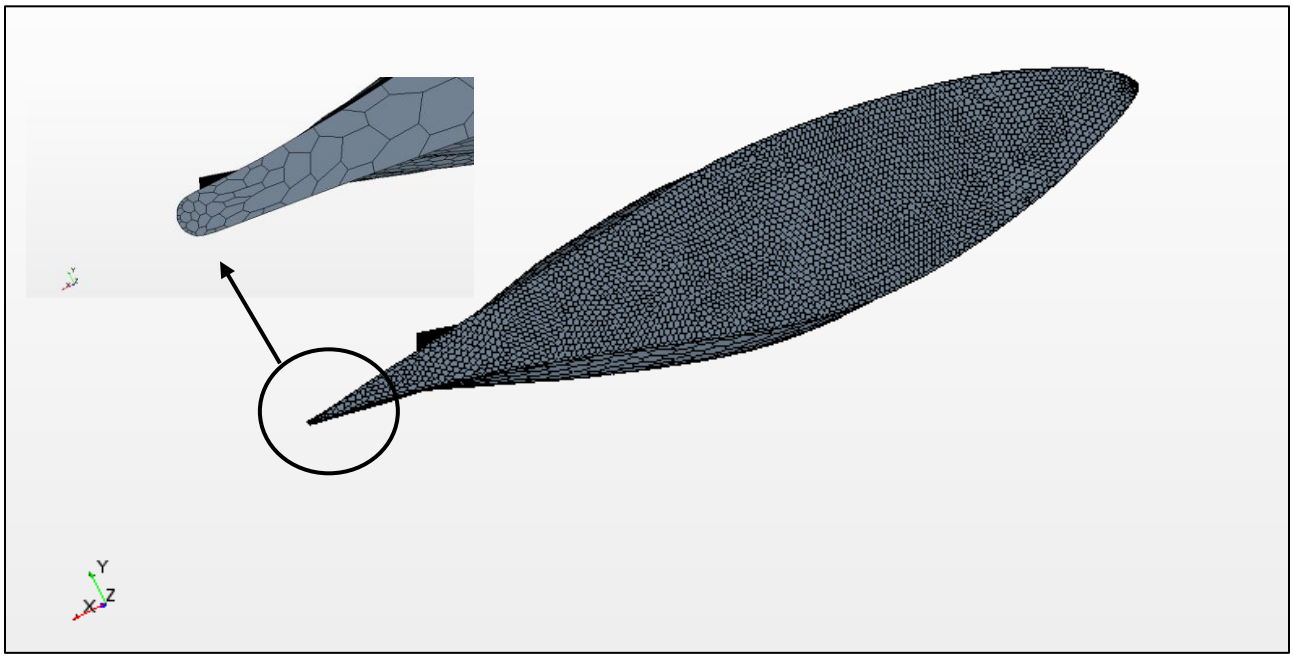

Figure 20 Curved/Blunt trailing edge

5.2. Modified NREL Phase VI blade

The aim of the present work is to validate the aerodynamic and acoustic performance of a wind turbine blade with leading edge tubercles. The leading edge of NREL Phase VI blade is modified with wavelength and amplitude as design parameters to mimic the flipper of a humpback whale. The wavelength and amplitude are chosen to be $0.25c_o$ and $0.025c_o$ respectively where maximum chord c_o=0.737m.

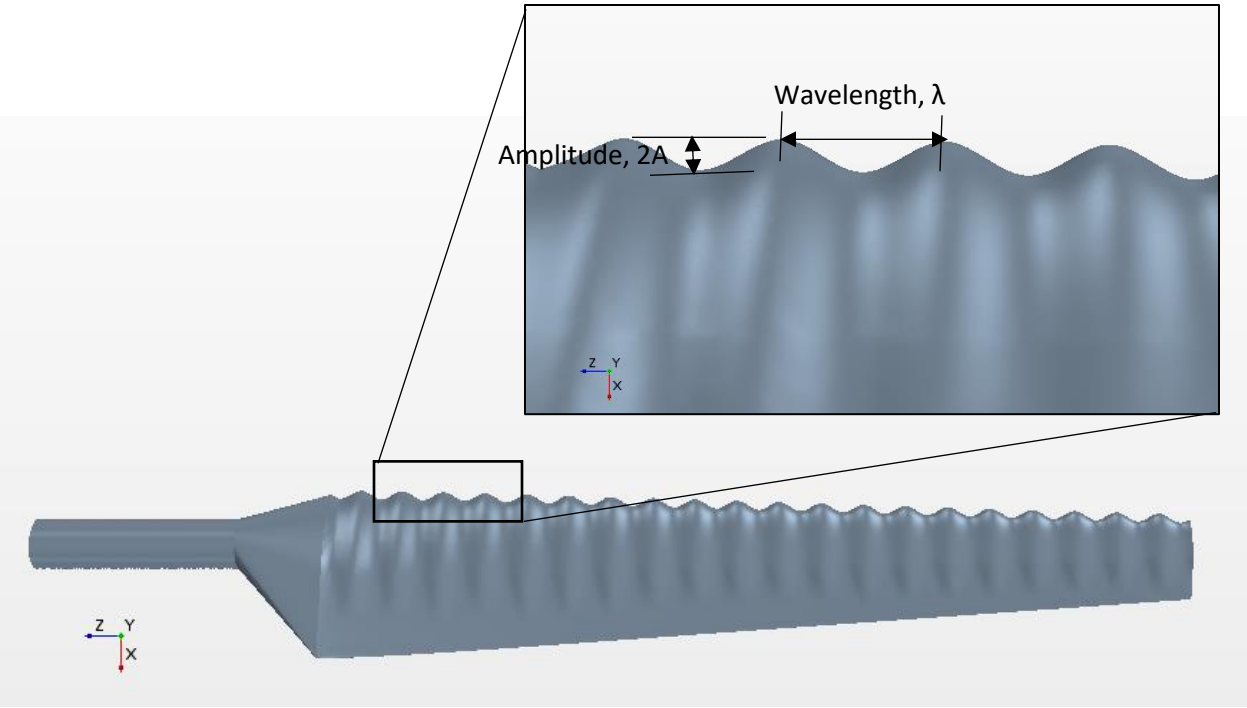

Figure 21 Modified Blade with sinusoidal leading edge

With the lack of proper literature to develop a blade with a sinusoidal leading edge, we resort to the method of trial and error to develop a blade with desired aerodynamic characteristics. Modified blade with airfoils at peak and trough of the leading edge is compared with the baseline S809 airfoil in Figure *22*

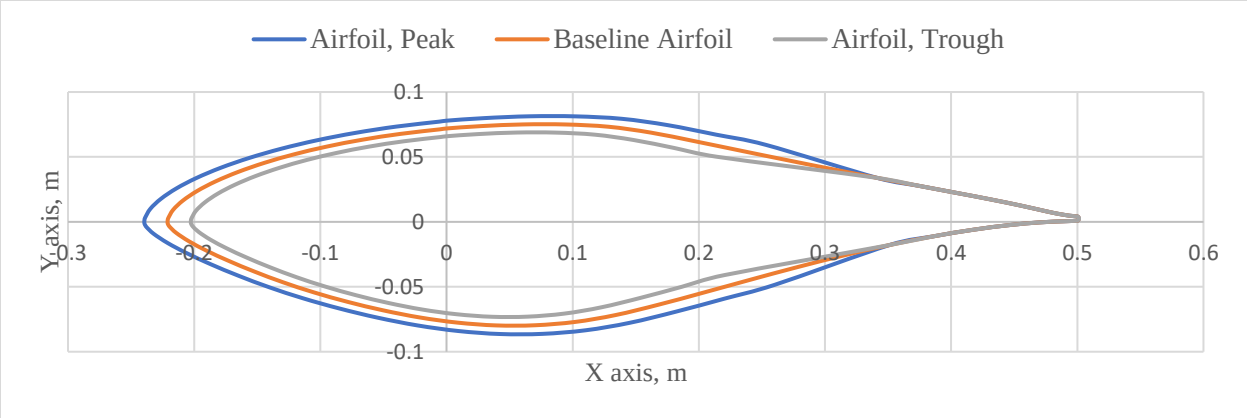

Figure 22 Peak and Trough comparison with baseline airfoil (c=0.737m)

5.3. Domain Setup

A semi-cylindrical domain is chosen for present work. Cylindrical domain will be advantageous and practical to define periodic boundary condition. To eliminate any blockage effects, the diameter of the domain is chosen to be 14R, where the span of the blade, R=5.029m. Inlet of the domain is 7R upstream from the blade and pressure outlet is 7R downstream of the blade. To implement periodic boundary condition, one surface of the domain is split into two equal dimension surfaces and a periodic interface is created among the split surfaces. All the boundaries of the domain can be seen in Figure 23. CAD of only one blade is generated using CAD tools in STAR CCM+ taking advantage of symmetry of two blade NREL Phase VI turbine. Results from this analysis can be applied to the second blade using periodic condition. The blade root is at the center of the coordinate system and span extends along negative Z-axis.

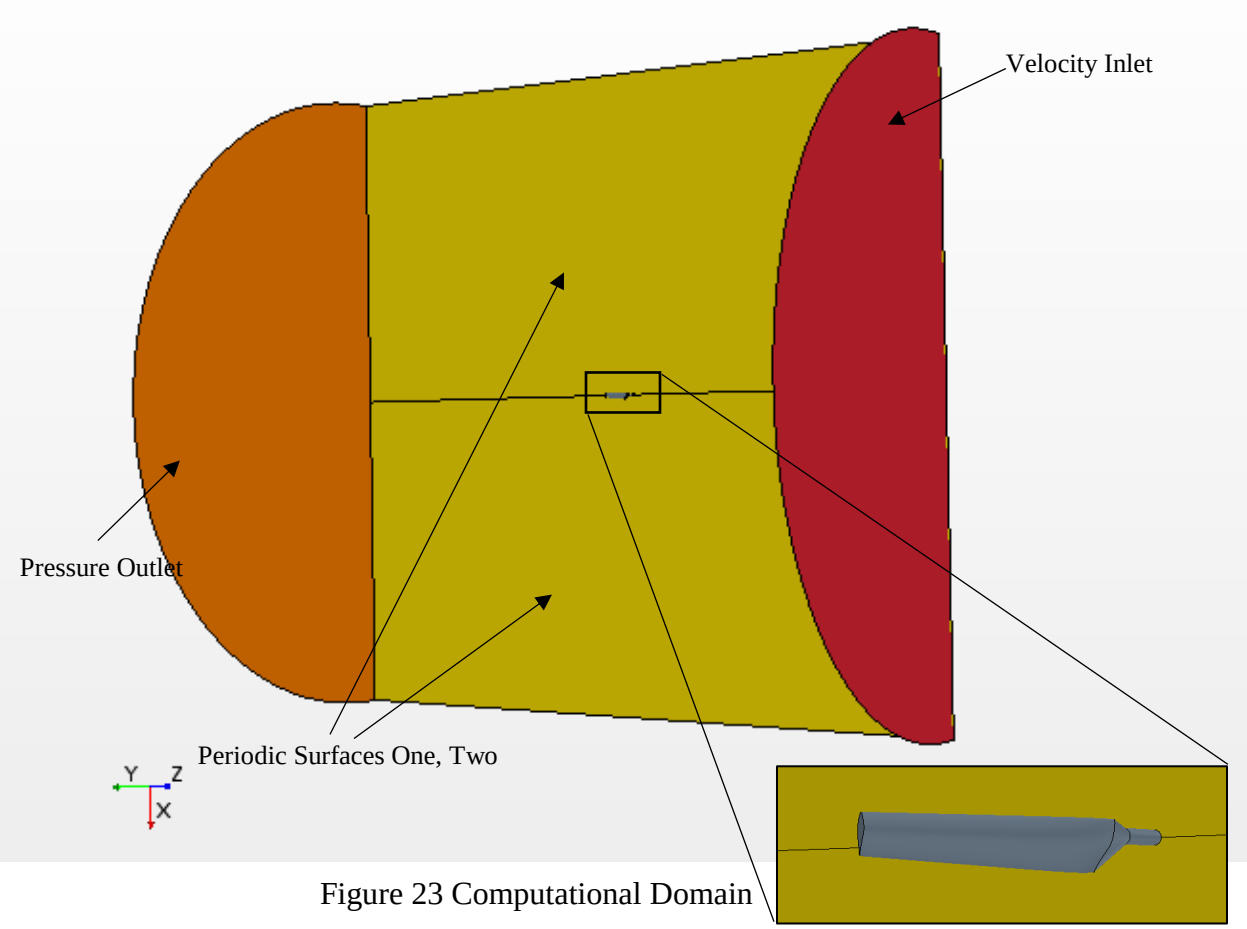

Figure 23 Computational Domain

6. Results

Prediction of near wall flow plays a major role in the accuracy of the solution. In the present work, Wall Y+ function is used to quantify the mesh quality near the surface and the capability of the prism layers to accurately capture the boundary layer flow. All Y+ wall treatment is used in the numerical analysis and y^+ value is desired to be below 5 to maintain the accuracy of the solution. A sample of y^+ values for the baseline and modified blade at 15m/s are shown in the figures below. It can be observed that a maximum of blade surface has a y+ value of less than 0.6 and a maximum y+ of 3 which is well below the required value of 5.

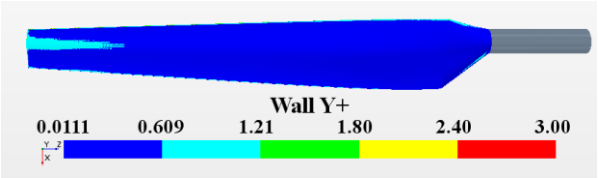

Figure 24 Wall y^+ on Pressure surface, Baseline Blade

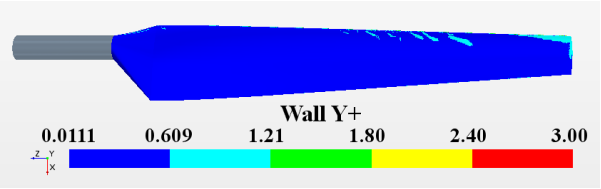

Figure 25 Wall y+ on suction, Baseline blade

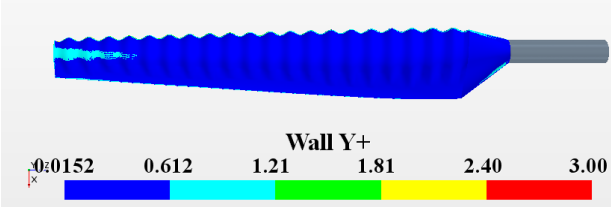

Figure 26 Wall y+ on pressure surface, Sinusoidal Blade

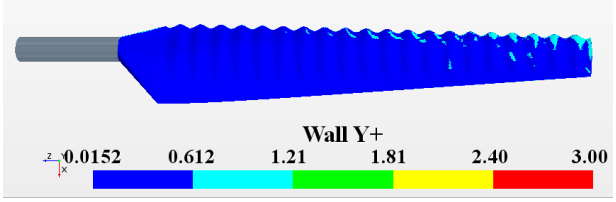

Figure 27 Wall y+ on Suction surface, Sinusoidal Blade

Numerical analysis is performed on the baseline blade and the modified blade with tubercles at five different wind speeds between 7m/s to 25m/s. To validate the numerical setup, results from the numerical simulation of the baseline blade are compared with the results from NREL experiment and other similar numerical analysis. We can understand from Figure 28 that present work shows good agreement with the experimental results at all wind speeds except 15m/s. The numerical model, following the pattern of all the other numerical references, underpredicts the torque at 15m/s when compared with experimental results.

6.1. Wind Turbine Torque

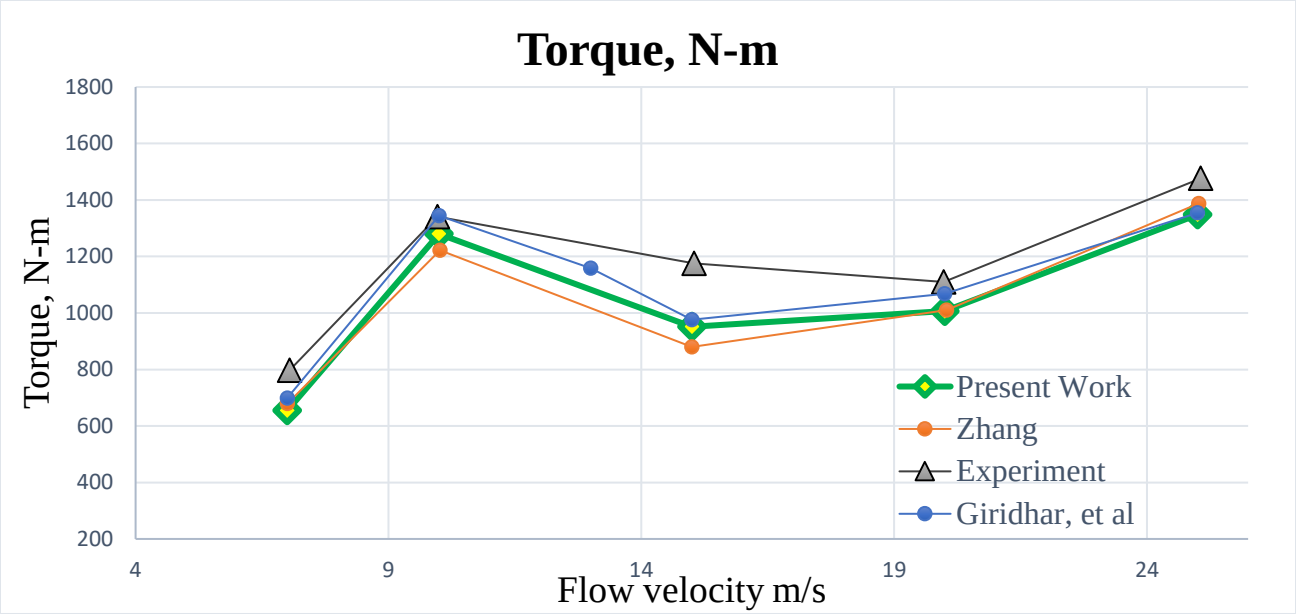

Figure 28 Present work Vs Literature Review

Referring to Figure 30, we can infer that the modified blade with sinusoidal leading edge underperforms at low wind speeds. At 10m/s the flow is mostly laminar over the baseline blade and this helps generate more torque. But in the modified blade, the laminar flow over the blade is disturbed due to the presence of the tubercles at the leading edge. These tubercles aid in the early separation of flow over the suction surface of the blade resulting in loss of torque. On the contrary, at moderate to high wind speed range of 15m/s to 25m/s flow is separated and turbulent over the suction surface of the baseline blade. In this situation, the leading-edge tubercles act as delta wings and generate high energy vortices at the trough of the tubercles. These vortices transfer the momentum to the boundary layer and help in delaying the flow separation over the suction surface, hence improving the power output.

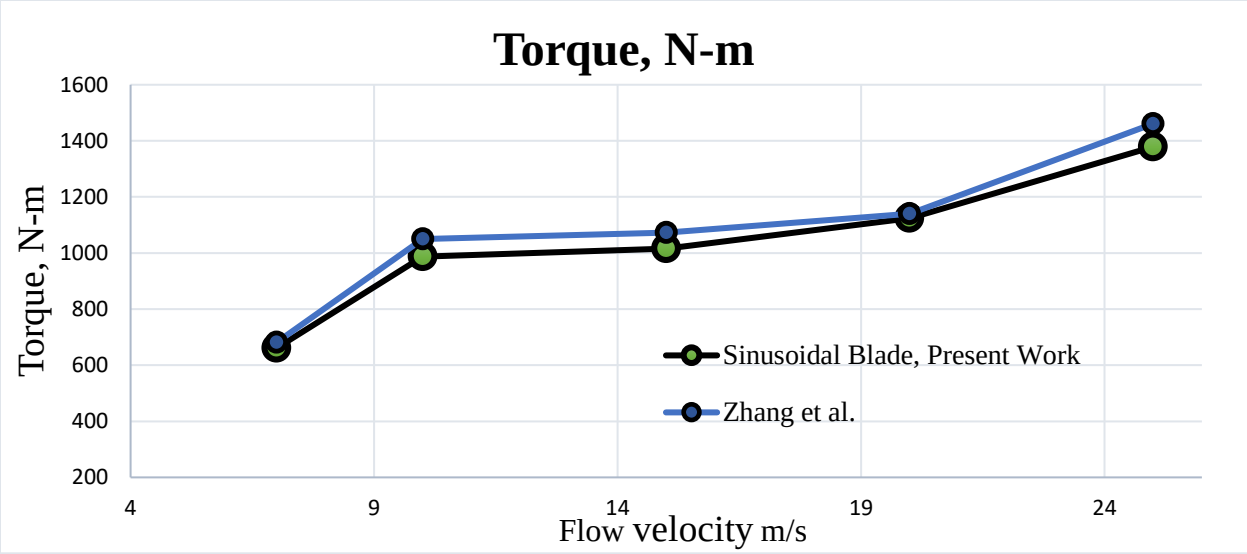

Figure 29 Present work Vs Zhang et al.

Figure *29* shows a comparison between the torque generated my sinusoidal leading edge blade in present work with work done by Zhang et al.[5] and we can observe that the results from present work show good agreement with the results from literature.

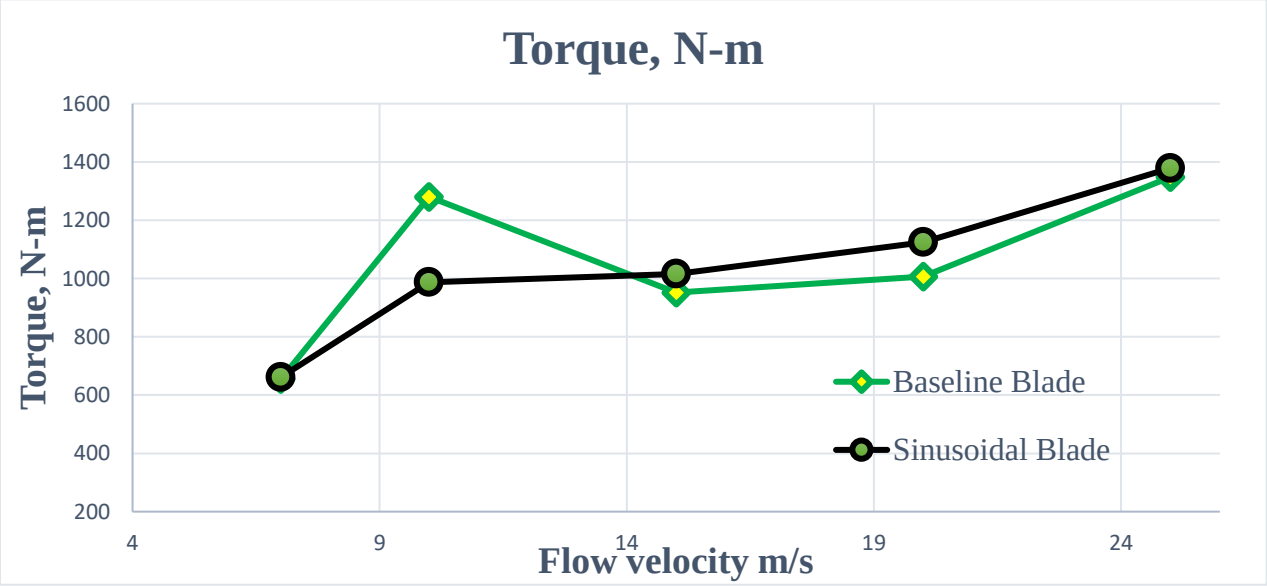

Figure 30 Baseline Blade Torque Vs Sinusoidal LE Blade

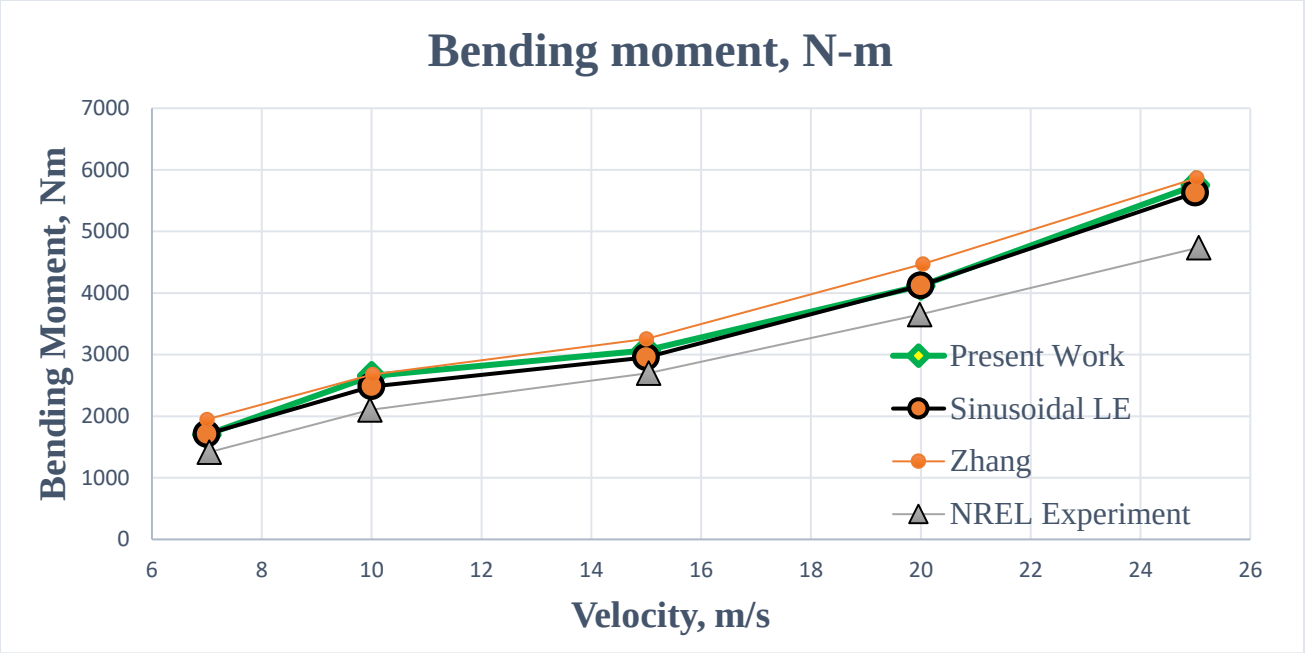

Figure 31 Bending moment at various wind speeds

We can observe from Figure 31 that modifying the leading edge has minimal to no effect on the root bending moment of the blade.

6.2. Acoustic Results

Acoustic performance of the blade in the present analysis are calculated using Curle noise source model. Curle model calculates the noise from the turbulent boundary layer flow over the blade and is suitable for low Mach number flow such as the present case. This model predicts the surface acoustic power to evaluate the local contribution to the total acoustic power per unit area of the body surface. We will compare the acoustic performance of baseline and sinusoidal blade at various wind speeds in this section.

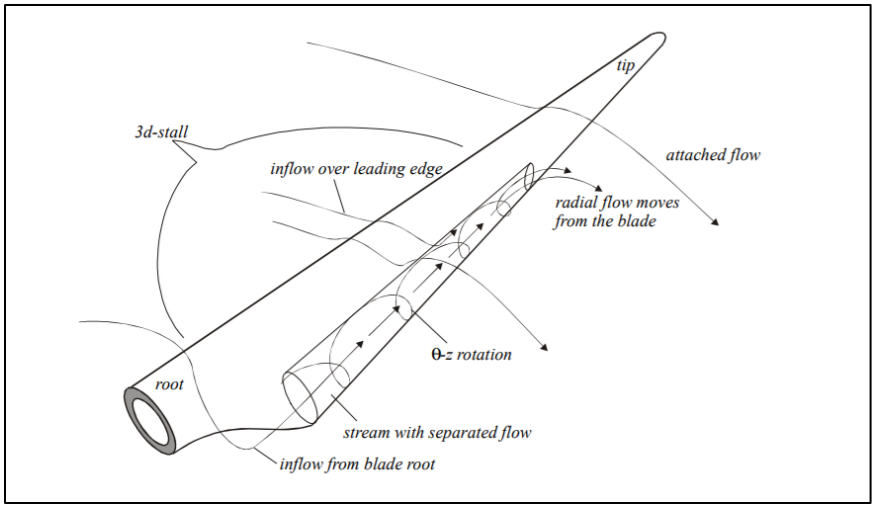

Figure 32 3D flow over a turbine blade

[26]

6.2.1. Results validation

It is important to validate the results from the numerical analysis with previous published results to evaluate the accuracy of present work. The surface acoustic power results are compared with Giridhar et al [28] and the coefficient of pressure plots are compared with experimental results from UAE experiment phase VI [11].

Surface acoustic power is compared with the literature at wind speeds of 7 m/s, 10 m/s and 15 m/s. It can be observed from Figure 33, Figure 34 and Figure 35 that surface acoustic power results from present work has a very good match with the literature at all wind speeds and hence the accuracy of present work is validated once again.

At 7 m/s

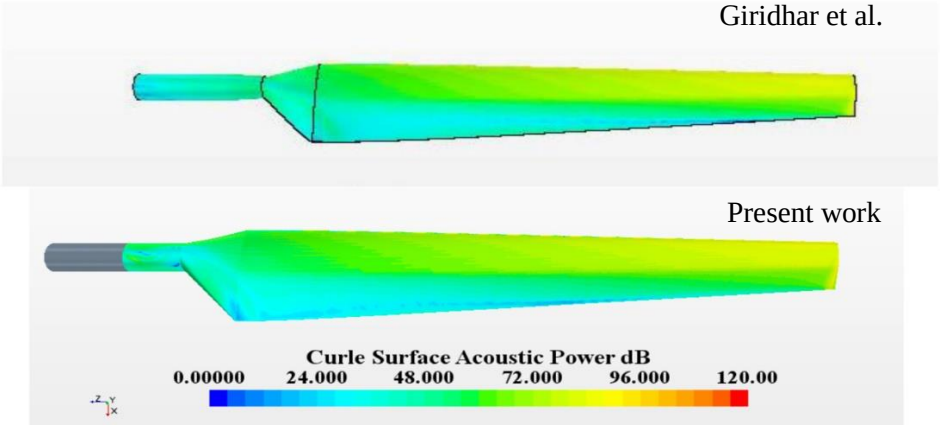

Figure 33 Surface acoustic power comparison at 7m/s

At 10 m/s:

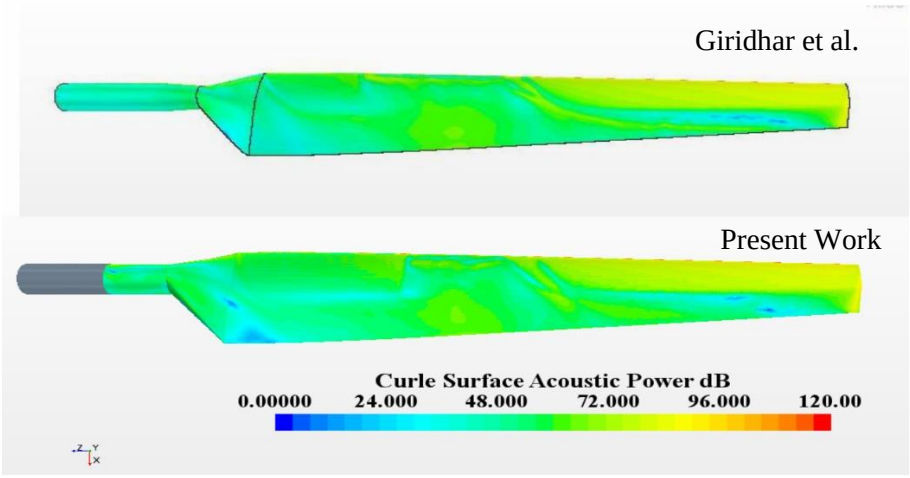

Figure 34 Surface acoustic power comparison at 10 m/s

At 15 m/s:

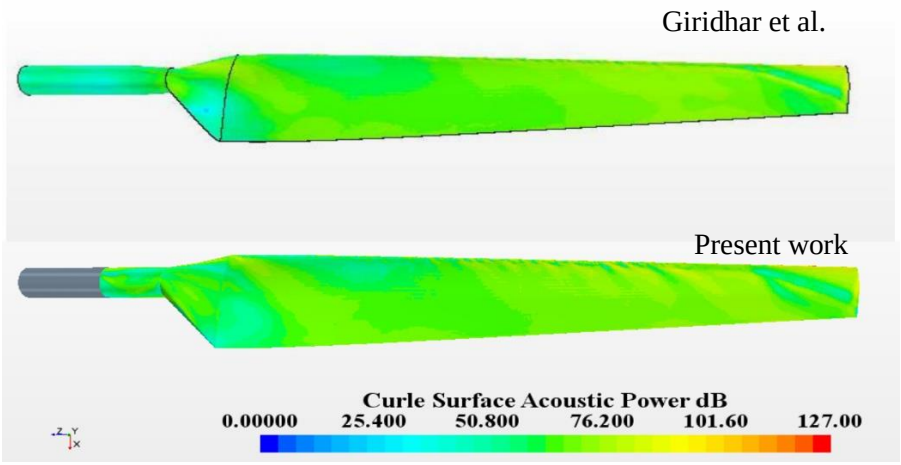

Figure 35 Surface acoustic power comparison at 15m/s

Coefficient of Pressure

7 m/s

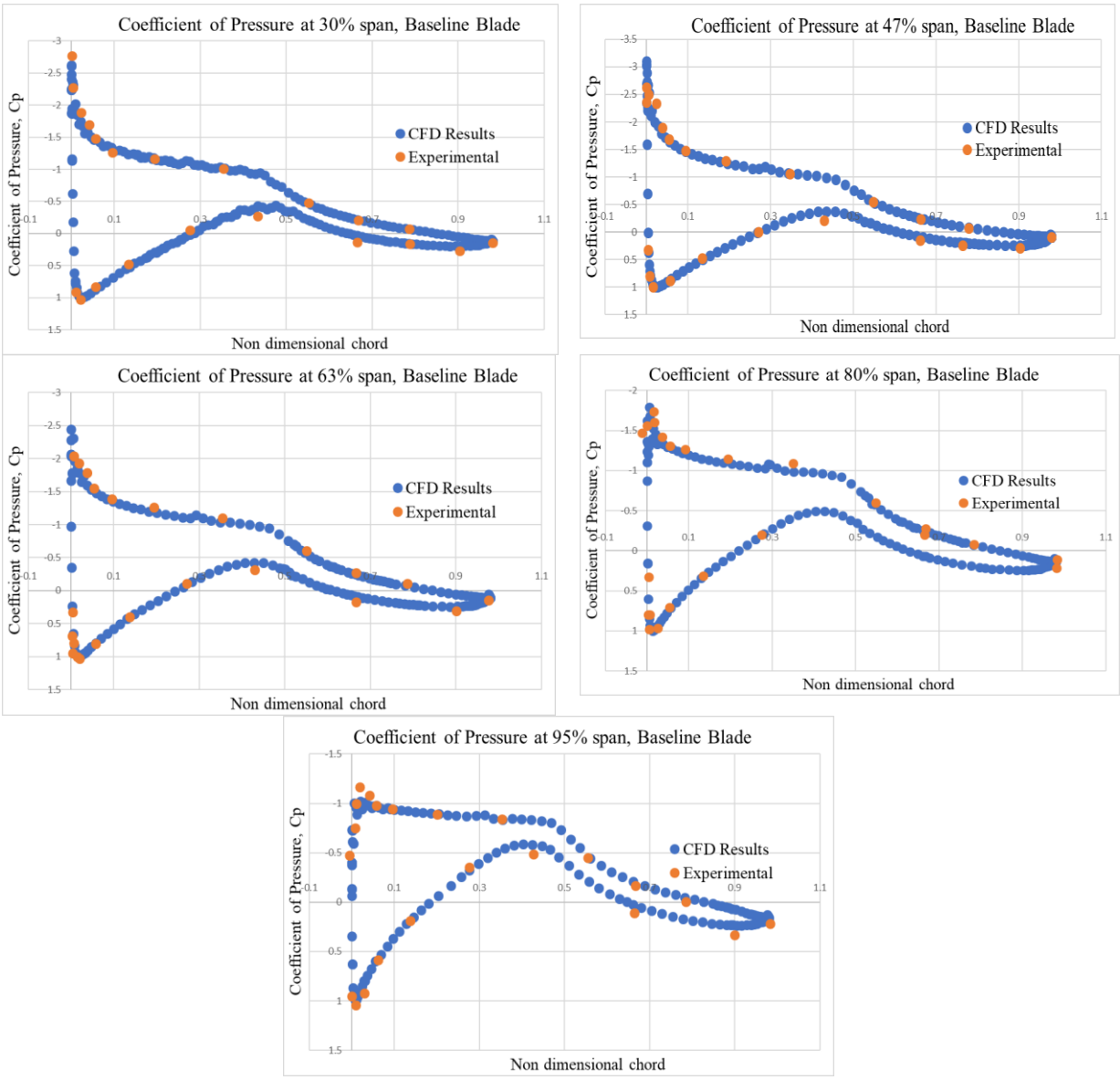

Figure 36 Coefficient of Pressure at 30%, 47%, 63%, 80% and 95% span. Baseline blade Vs Experiment (7m/s)

Coefficient of pressure is computed for the baseline blade along the span at five different locations namely 30%R, 47%R, 63%R, 80%R and 95%R. These calculated results are then compared with experimental results from UAE Phase VI [11]. We can observe from Figure 36 that all the calculations show a good agreement with the experimental results and hence a good prediction of torque.

At 15 m/s

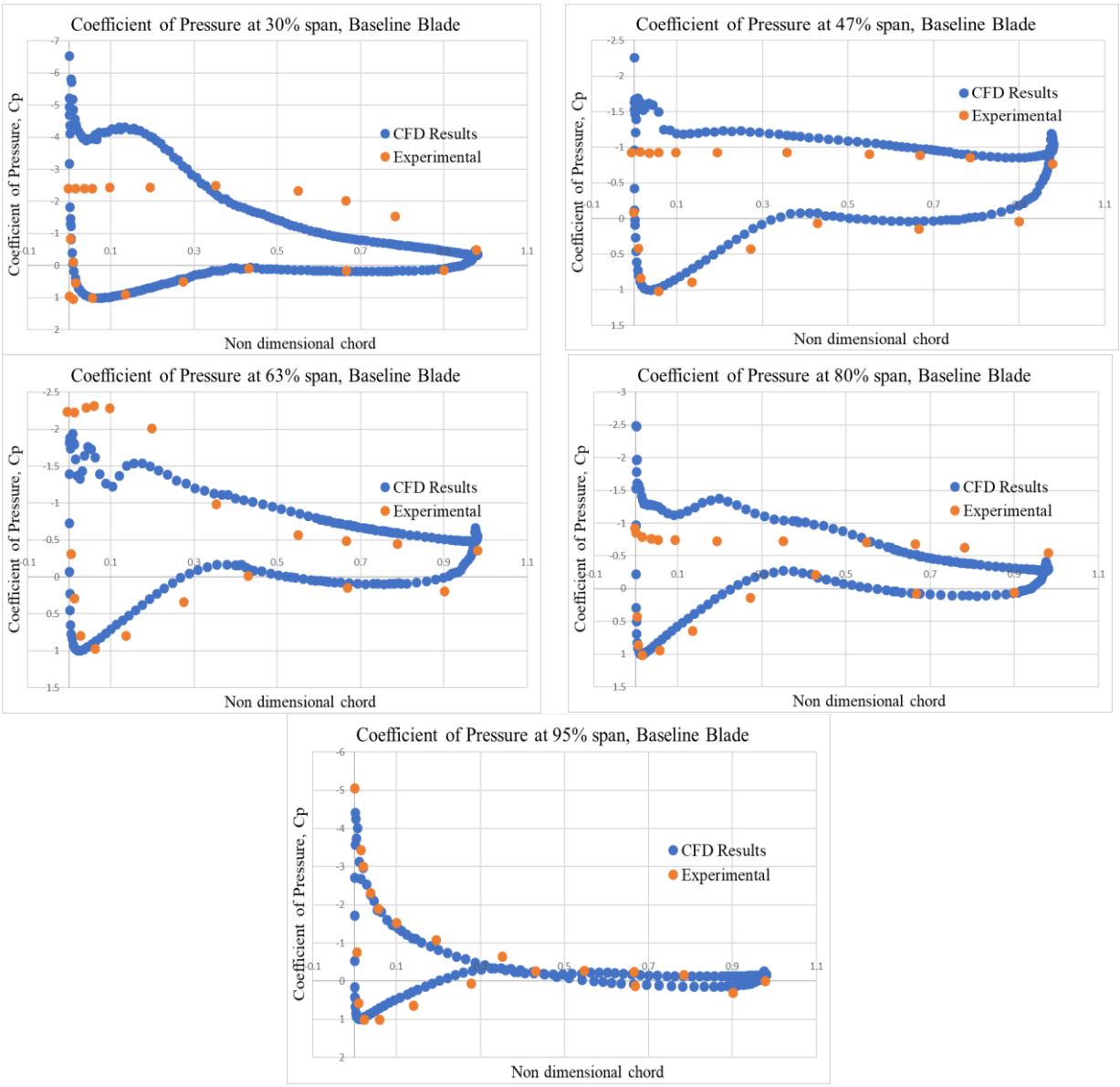

Figure 37 Coefficient of Pressure at 30%, 47%, 63%, 80% and 95% span. Baseline blade Vs Experiment (15m/s)

At 15m/s the numerical method under predicts the torque when compared with the experimental results and the same pattern is observed in coefficient of pressure calculations from Figure 37 where there is a disagreement in pressure prediction on suction surface at 30%, 47%, 63% and 80%.

6.2.2. At wind Speed of 7 m/s

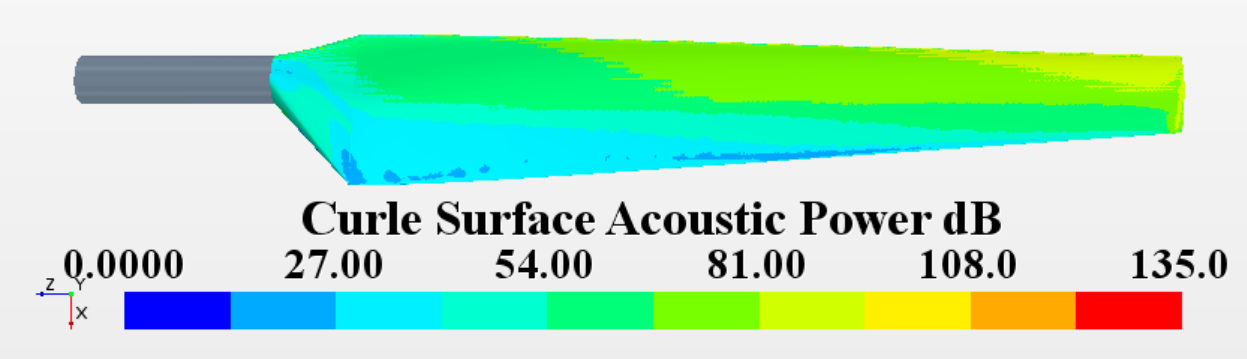

Figure 38 Acoustic Power distribution on suction surface of baseline blade, 7m/s

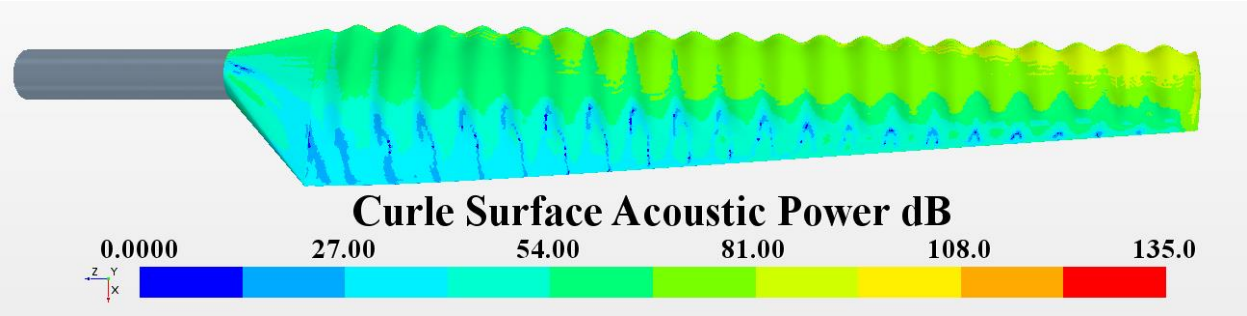

Figure 39 Acoustic power on Suction surface of the modified blade, 7m/s

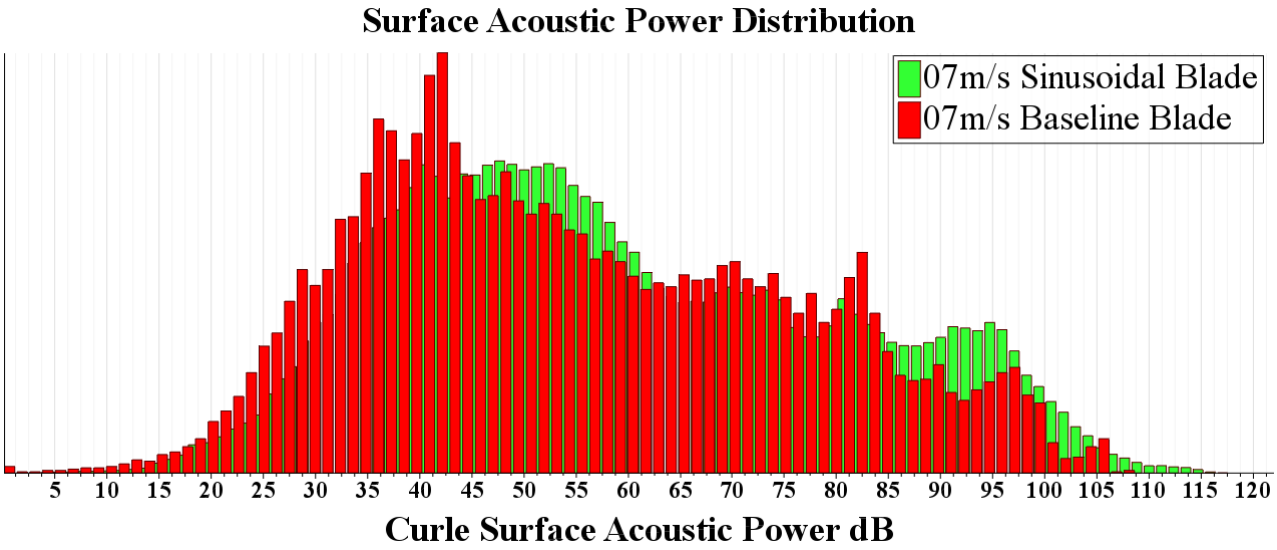

Figure 40 Acoustic power Distribution at 7m/s Baseline VS Sinusoidal Blade

Figure 40 shows the comparison of surface acoustic power between the two blades in a histogram plot where the X-axis represents the noise intensity and y-axis represents the frequency of noise. At 7m/s the noise is evenly distributed across the scale compared to other wind speeds with 43dB being the most frequent noise level compared to 49dB for the modified blade. Though there is a major difference in the most frequent noise level in both the blades, the average surface acoustic power of the modified blade is 58.25dB which is only higher than the 58.09dB average of baseline blade by a very small percentage. We can observe from Figure *38* and Figure *39* that the root of the blade is quitter and noise level increases from the root and along the spanwise direction with the tip being the noisy part of the blade for both the models.

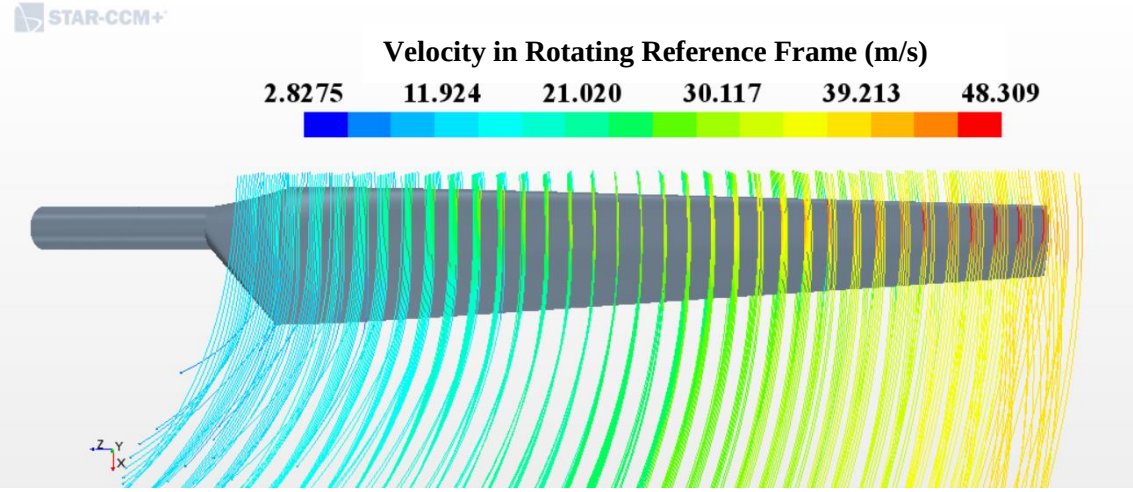

Figure 41 Flow over suction surface at 7 m/s, Baseline blade

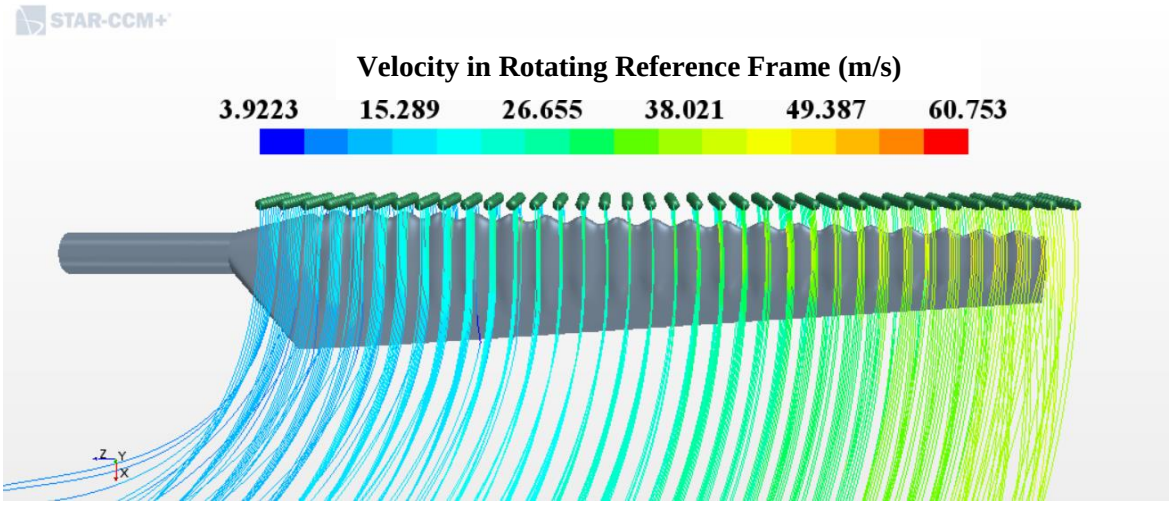

Figure 42 Flow over suction surface at 7 m/s, Sinusoidal Blade

Figure *41* and Figure *42* depicts a streamline representation of flow over the wind turbine blades at 7 m/s. We can observe from the figures that the flow around the blade at this velocity is laminar and there is no separation on the suction surface. As flow is laminar and attached to the blade along the chord the noise level generated at 7 m/s is also low.

6.2.3. At wind Speed of 10 m/s

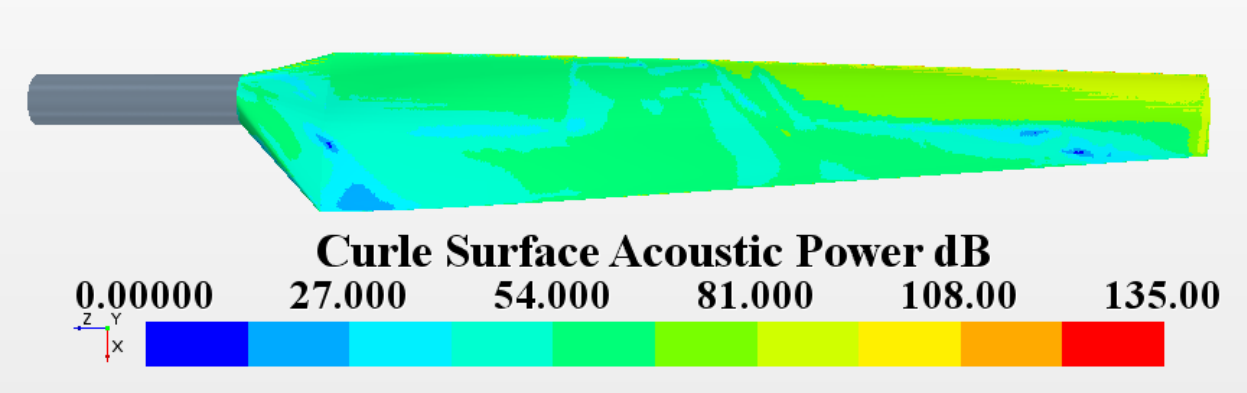

Figure 43 Acoustic power distribution on suction surface of baseline blade, 10m/s

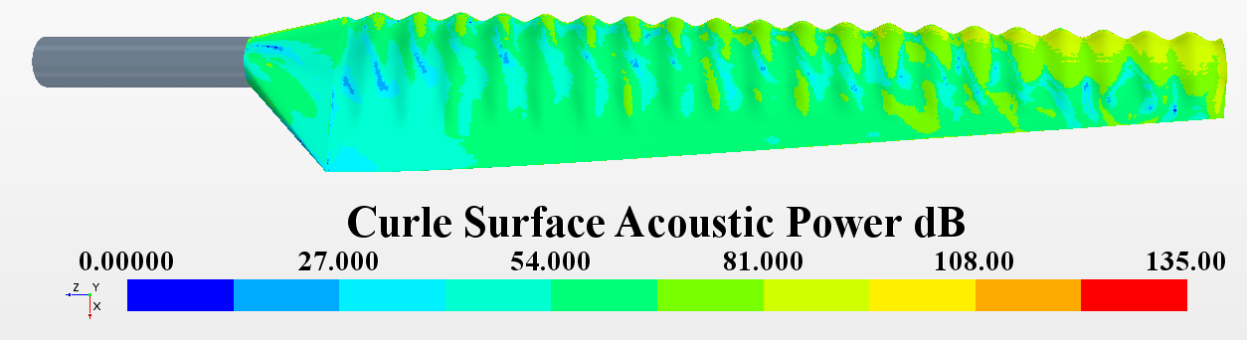

Figure 44 Acoustic power on Suction surface of the modified blade, 10m/s

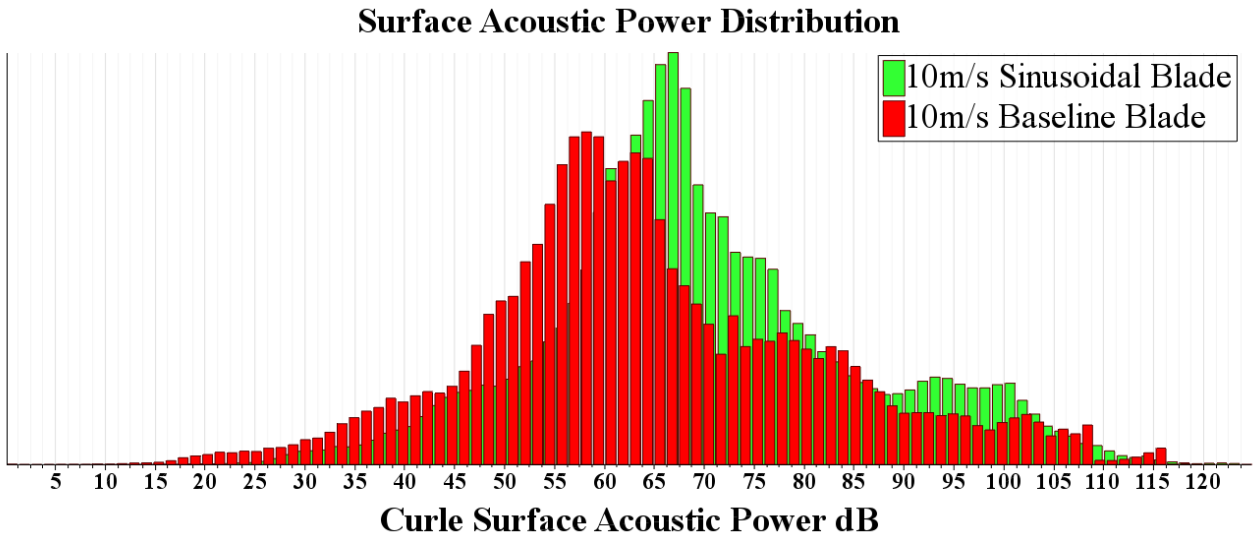

Figure 45 Acoustic power Distribution at 10m/s Baseline VS Sinusoidal Blade

Histogram of surface acoustic power comparison at 10m/s has a major visual difference in the frequency of noise level with most frequent noise level is 57dB and 69 dB for baseline model and Sinusoidal model respectively. The average surface acoustic power of baseline blade is 58.58dB whereas the average for the sinusoidal blade is 60.51dB with a difference of 1dB between two blades which is a considerable drawback for the modified blade as noise is measured in logarithmic scale.

This increase in noise generated by the modified blade can be attributed to the vortices generated by the leading-edge tubercles making the flow more turbulent, whereas flow over the baseline blade is laminar at the speed of 10m/s.

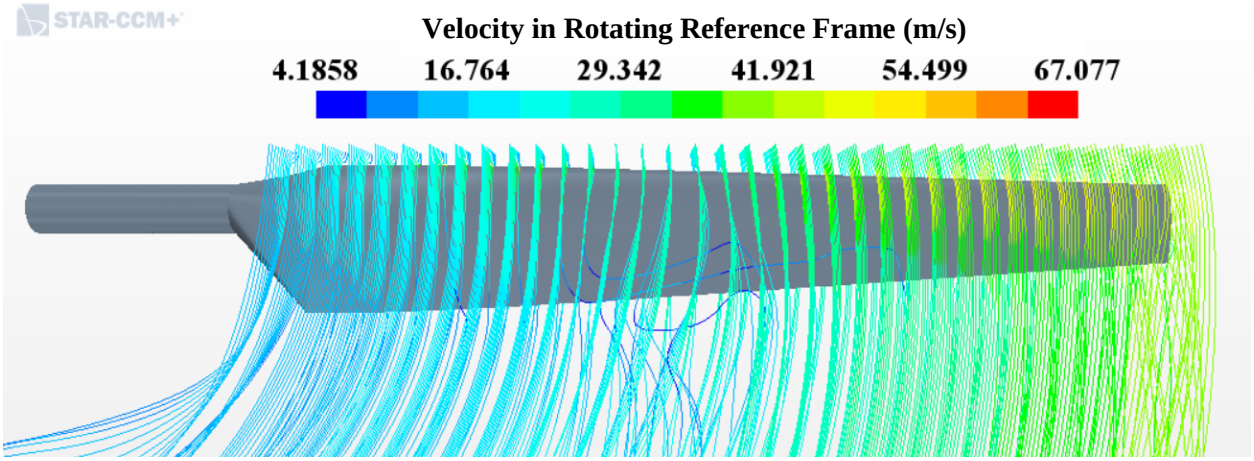

Figure 46 Flow over suction surface at 10 m/s, Baseline blade

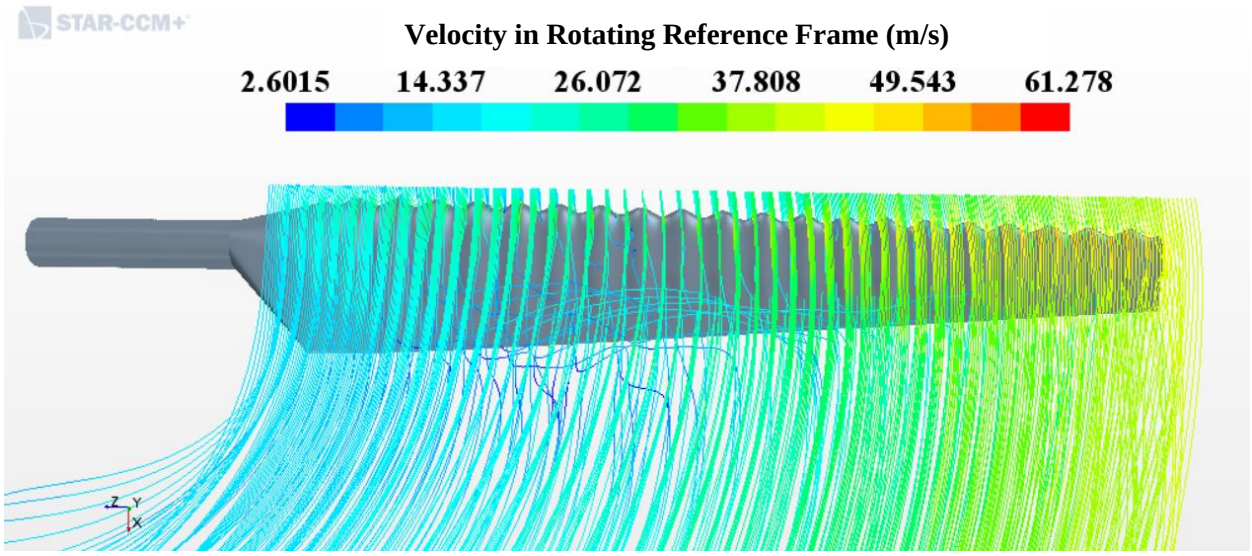

Figure 47 Flow over suction surface at 10m/s, Sinusoidal Blade

At 10m/s flow begin its transition from laminar to turbulent and the same can be observed from Figure *46* and Figure *47* thought separations happens only in the small area on the suction surface. Observing the flow on the baseline blade, separation on the blade is very limited but when

compared with the flow over the sinusoidal blade, the modified blade has a larger separation region than the baseline. This can be explained by the presence of tubercles in the modified blade which create a disturbance in the flow and this leads to early separation because of the weakened boundary layer. Due to this, the modified blade generates less torque at 10m/s compared to a baseline blade and can be noticed in Figure 30. This flow behavior also explains the sudden jump in noise generated by sinusoidal blade between 7m/s and 10m/s which can be observed in Figure *64*.

6.2.4. At wind Speed of 15 m/s

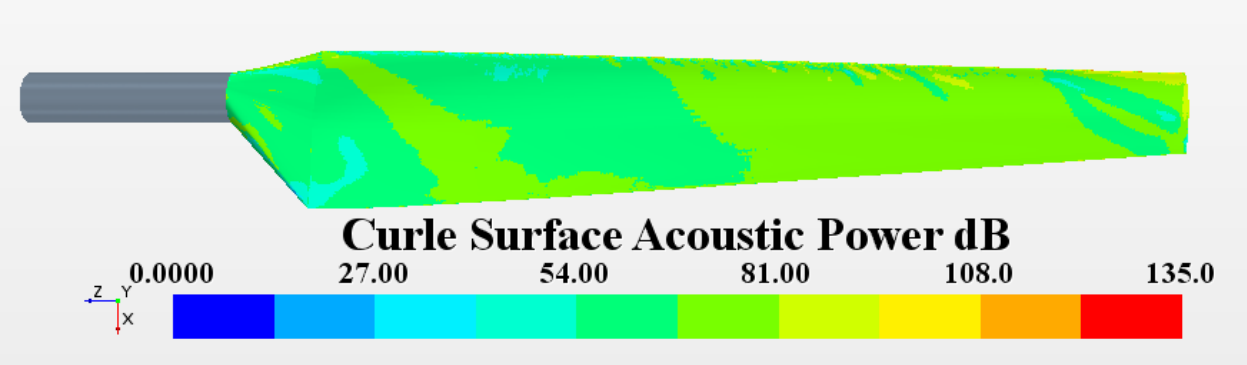

Figure 48 Acoustic power distribution on suction surface of baseline blade, 15m/s

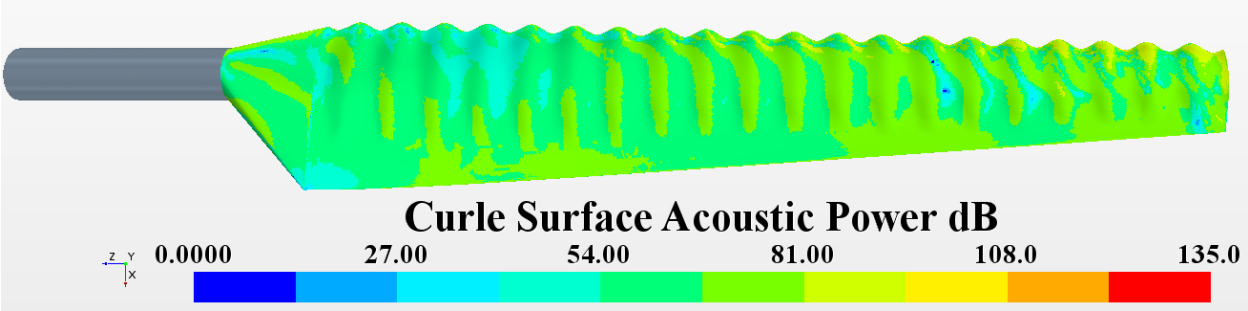

Figure 49 Acoustic power on Suction surface of modified blade, 15m/s

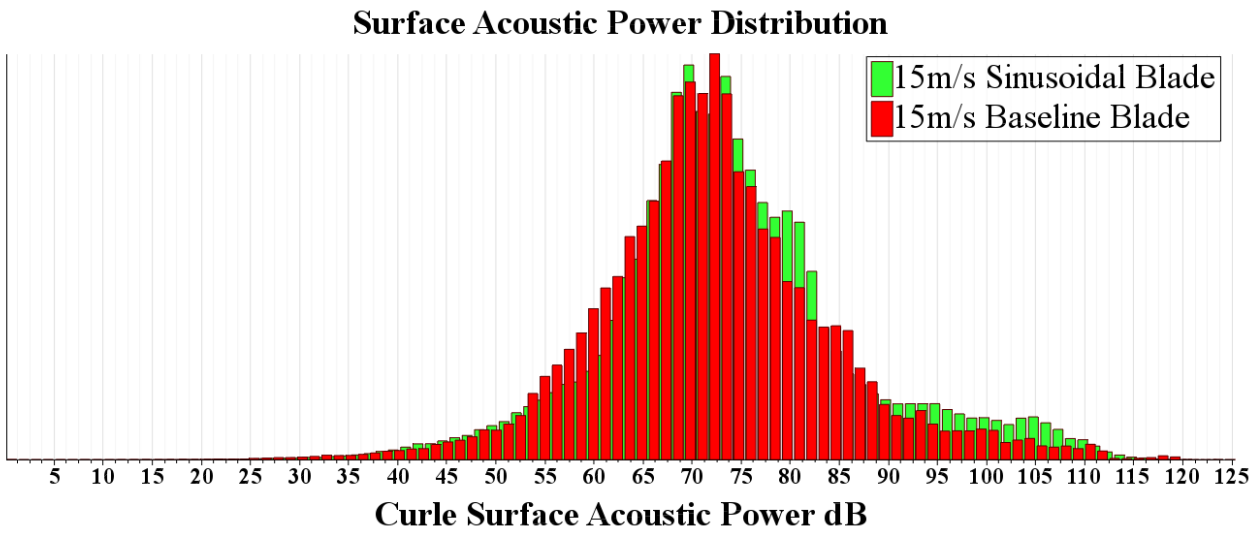

Figure 50 Acoustic power Distribution at 15m/s Baseline VS Sinusoidal Blade

At 15m/s we can observe that both the blades have almost same most-frequent noise level of 73dB, with the average acoustic power of baseline blade and the modified blade are 65.668dB and 64.799dB respectively. Though modified blade is relatively noisy at low wind speeds, the average acoustic power of baseline blade is 0.87dB more than the modified blade at 15m/s with almost similar distribution of acoustic power across the blade. Increase in noise generated by baseline blade can be explained by increase in turbulence over the suction surface caused due to the separation of the boundary layer.

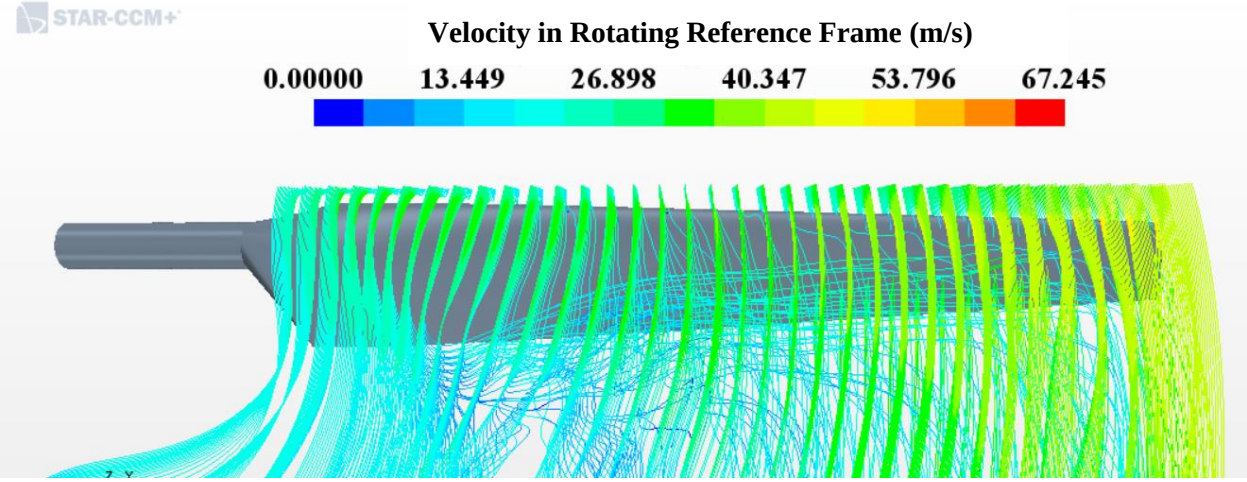

Figure 51 Flow over suction surface at 15 m/s, Baseline Blade

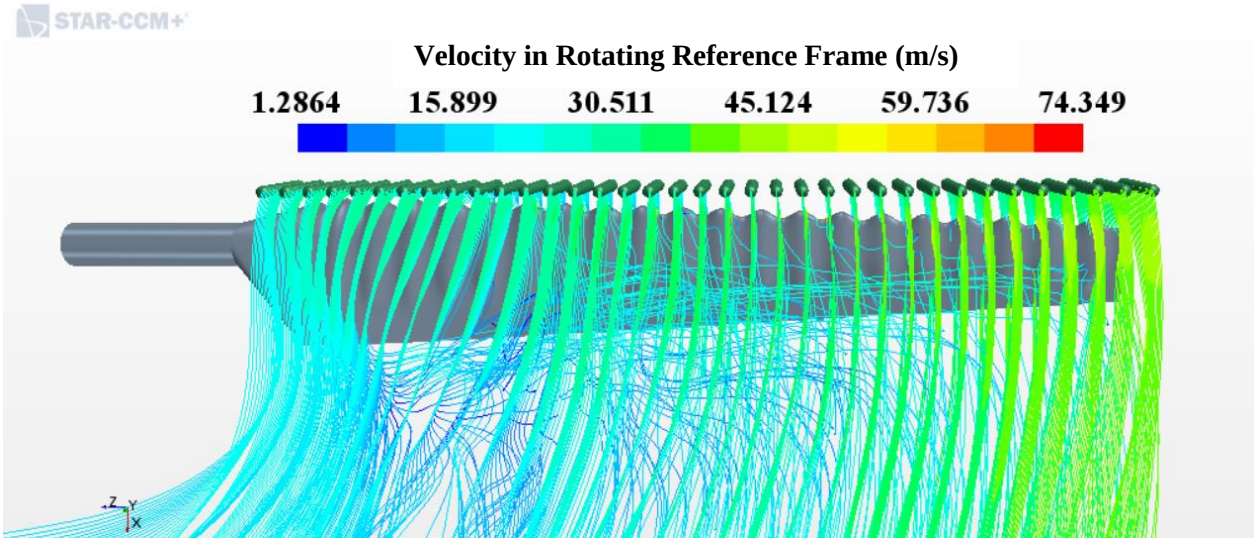

Figure 52 Flow over suction surface at 15 m/s, Sinusoidal Blade

At 15m/s majority of the flow is turbulent on the baseline and modified blades. In baseline blade separation starts at about 35% of the span and increases as we move towards the tip of the blade. Similarly, separation in the modified blade starts at the same span location but does not increase as we move towards the tip and is limited to the latter half of the blade chord. The presence of tubercles, at high wind speeds create counter-rotating vortices at the trough of the tubercles which energizes the boundary layer flow and delay the flow separation. This phenomenon helps the

modified blade to generate more torque than the baseline blade as observed in Figure 30. Less turbulence by modified blade can also explain relatively less noise generated by it when compared to the baseline blade.

6.2.5. At wind Speed of 20 m/s

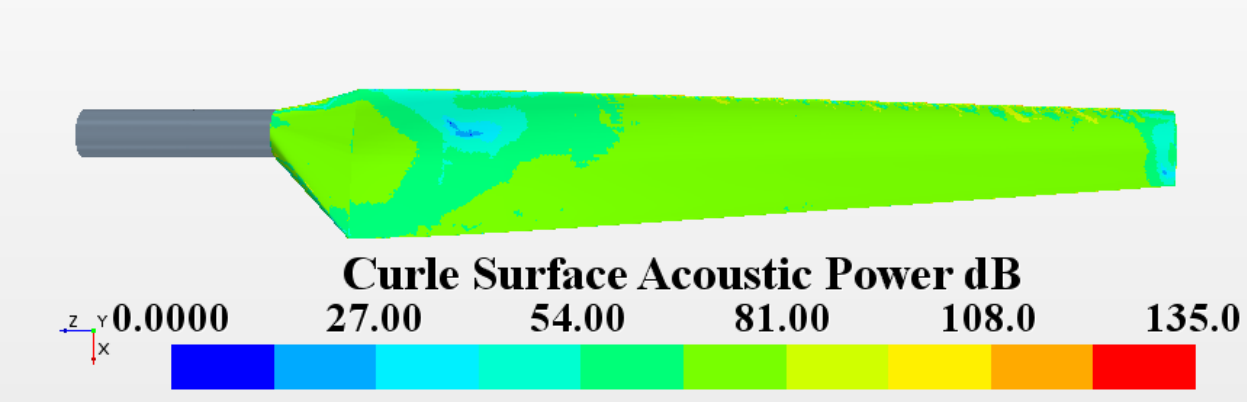

Figure 53 Acoustic power distribution on suction surface of baseline blade, 20m/s

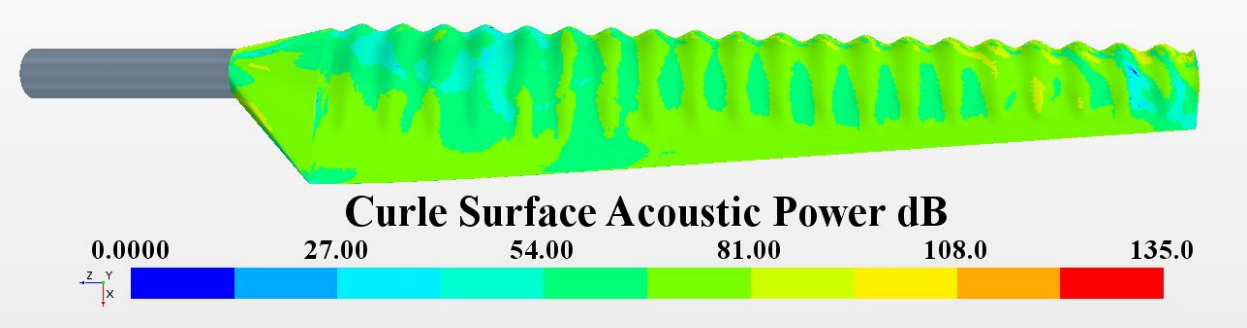

Figure 54 Acoustic power on Suction surface of modified blade, 20m/s

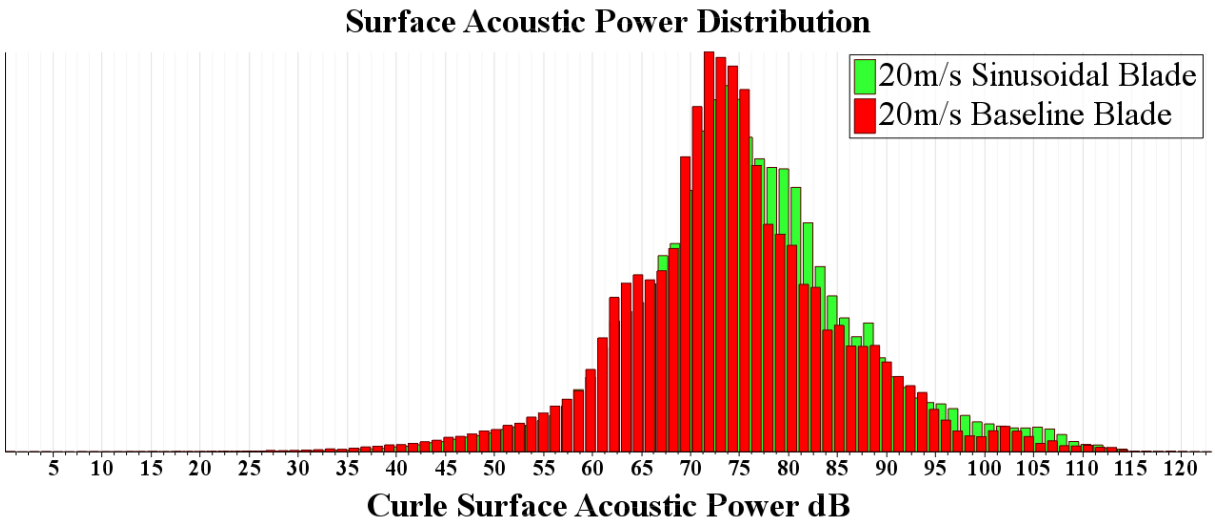

Figure 55 Acoustic power Distribution at 20m/s Baseline VS Sinusoidal Blade

At 20 m/s we can observe that both the models have similar acoustic performance but generate more noise when compared to 15m/s and 10 m/s. both the blades have the most frequent noise level of 75dB and an average noise level of 67.43dB for the baseline blade and 67.31dB for the modified model. Thought the modified blade does generate less noise than the baseline, the difference in the intensity is very small and can be considered identical.

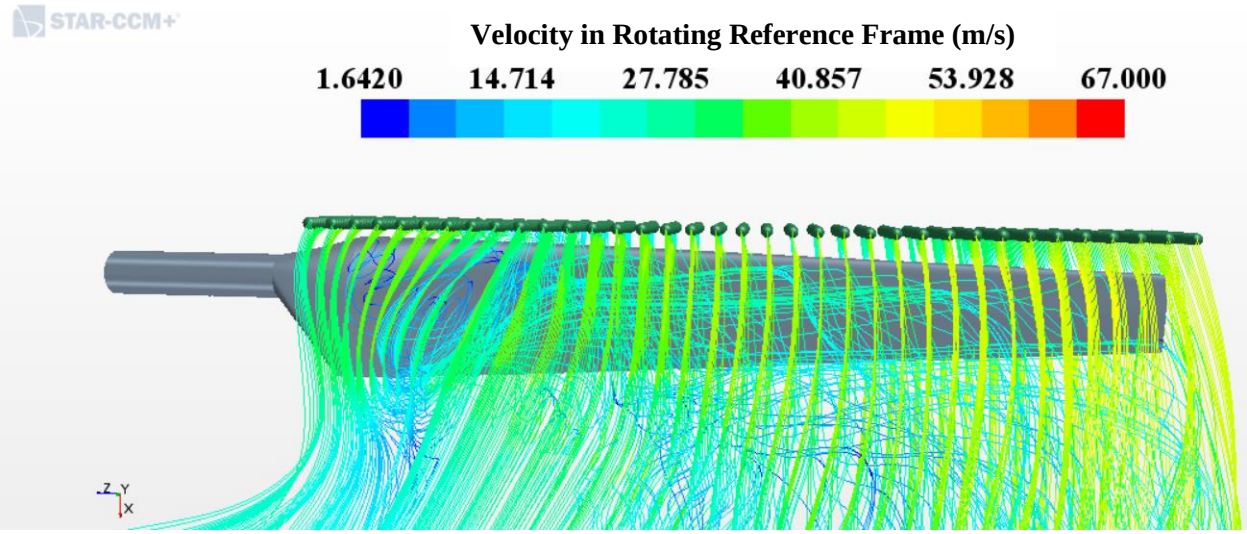

Figure 56 Flow over suction surface at 20 m/s, baseline blade

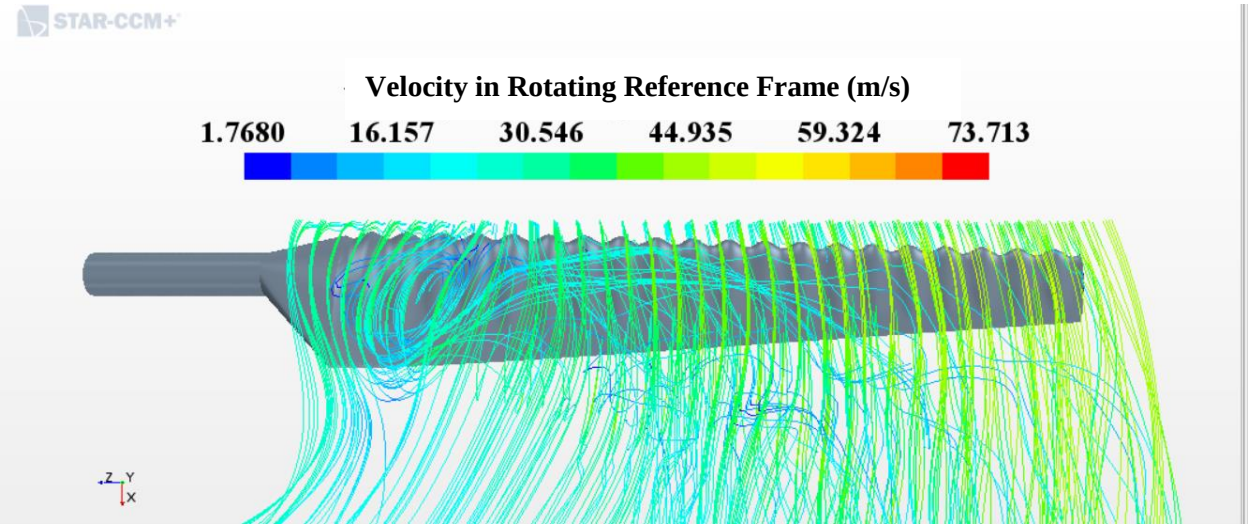

Figure 57 Flow over suction surface at 20 m/s, Sinusoidal blade

Improved performance of modified blade continuous from 15m/s to 20m/s. In Figure *56* and Figure *57* we can observe that the major part of the flow on suction surface is separated. As the flow is separated till the tip of the blade in the baseline blade, the tubercles in the sinusoidal leading-edge blade help the flow to be attached to the blade along 80-100% span. This again results in more torque generation when compared with the baseline blade.

6.2.6. At wind Speed of 25 m/s

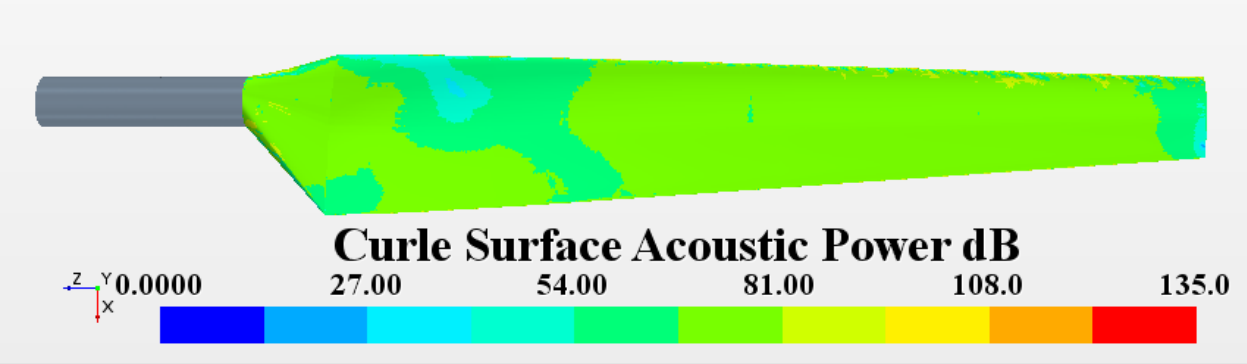

Figure 58 Acoustic power distribution on suction surface of baseline blade, 25m/s

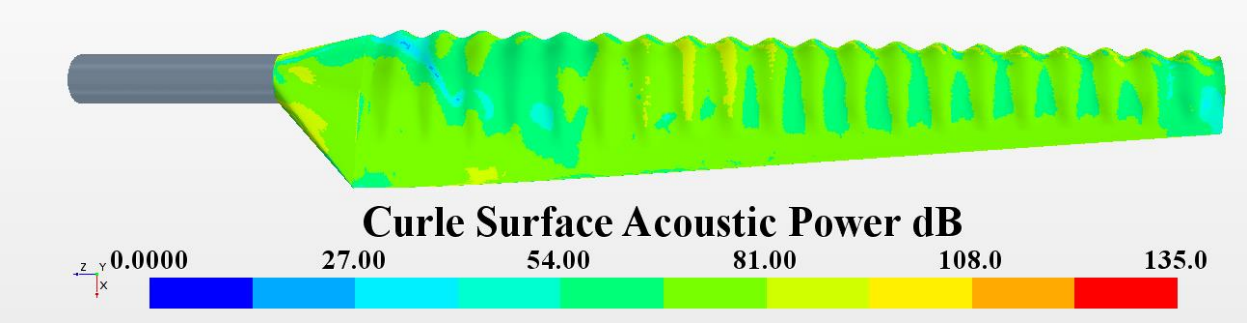

Figure 59 Acoustic power on Suction surface of modified blade, 25m/s

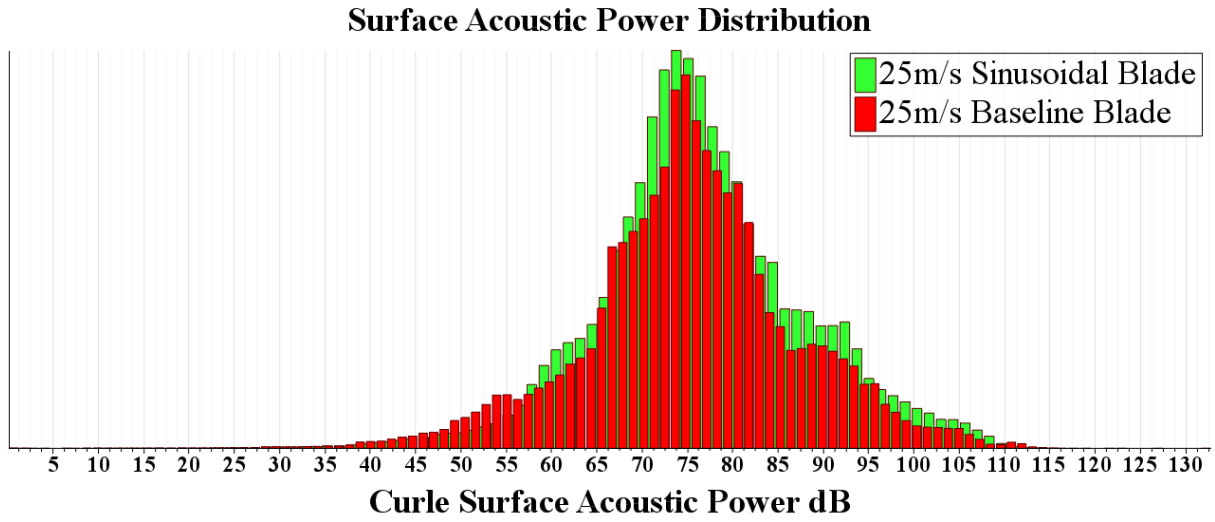

Figure 60 Acoustic power Distribution at 25m/s Baseline VS Sinusoidal Blade

Acoustic behavior of both the models at 25 m/s is similar to the behavior at 20 m/s. most frequent noise level is 75dB for both blades and have the same average noise level of 69dB. It can again be observed that the noise at the root of the blade is low and the tip generates a noise level of over 100dB.

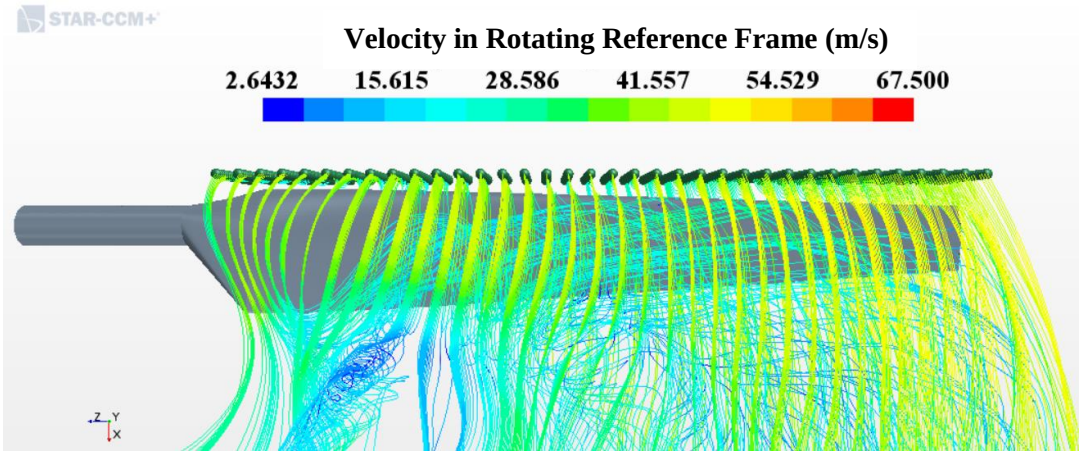

Figure 61 Flow over suction surface at 25 m/s, baseline blade

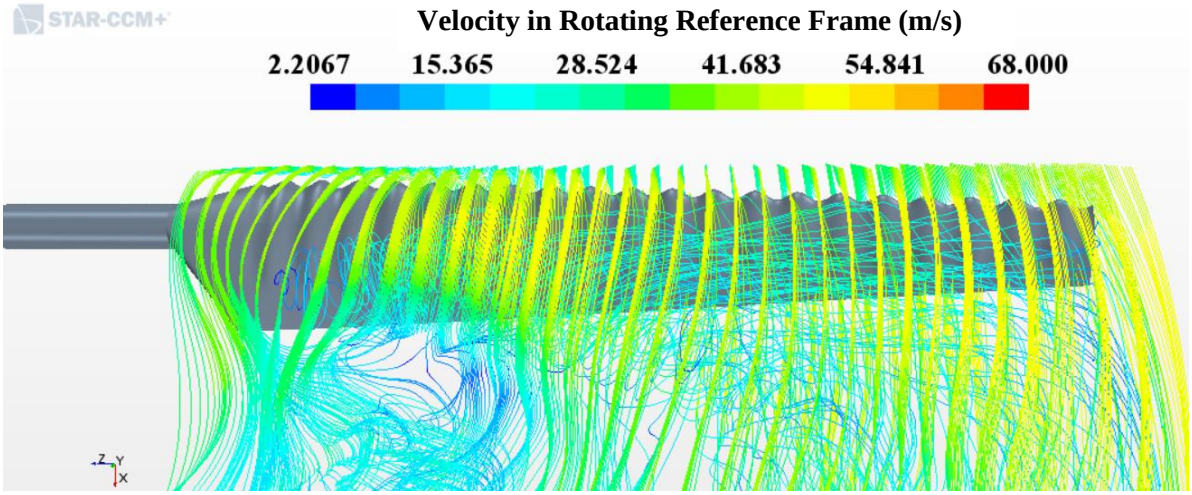

Figure 62 Flow over suction surface at 25 m/s, Sinusoidal Blade

Flow at 25 m/s is highly turbulent and no major differences can be observed between the baseline model and the modified blade. Same behavior reflects in the power output as both the models generate similar torque output.

Average, dB	7 m/s	10 m/s	15 m/s	20 m/s	25 m/s
Baseline	58.099	59.587	65.668	67.436	69.093
Sinusoidal	58.254	60.517	64.799	67.318	69.019

Table 7 Average Surface Acoustic Power

At higher wind speeds of 20m/s and 25m/s the surface acoustic power increases with speed for both the models but the average acoustic power of both the blades is similar and the modified blade with tubercles is not quitter compared to the baseline blade, which contradicts the hypothesis that the modified blade has better acoustic performance.

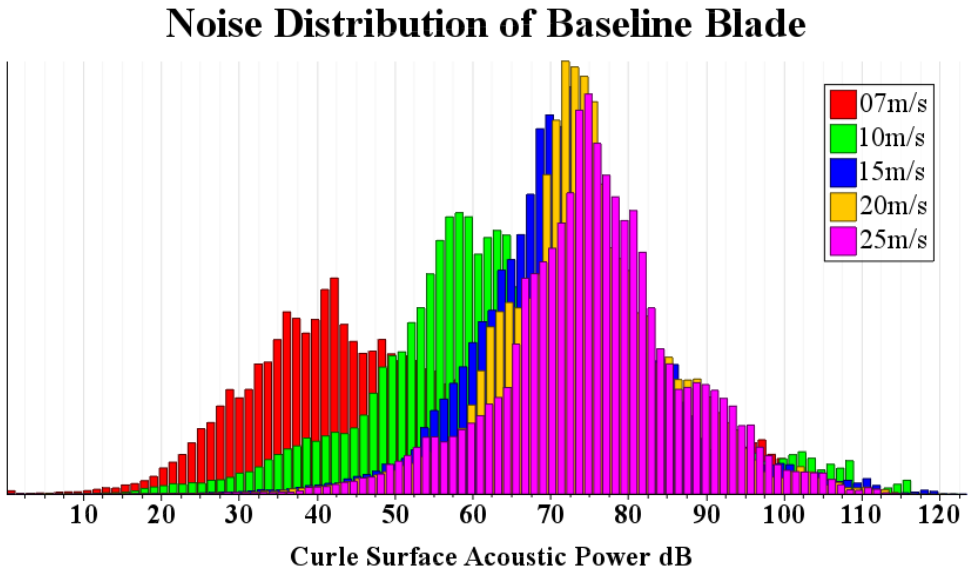

Figure 63 Noise frequency distribution at various speeds, Baseline Blade

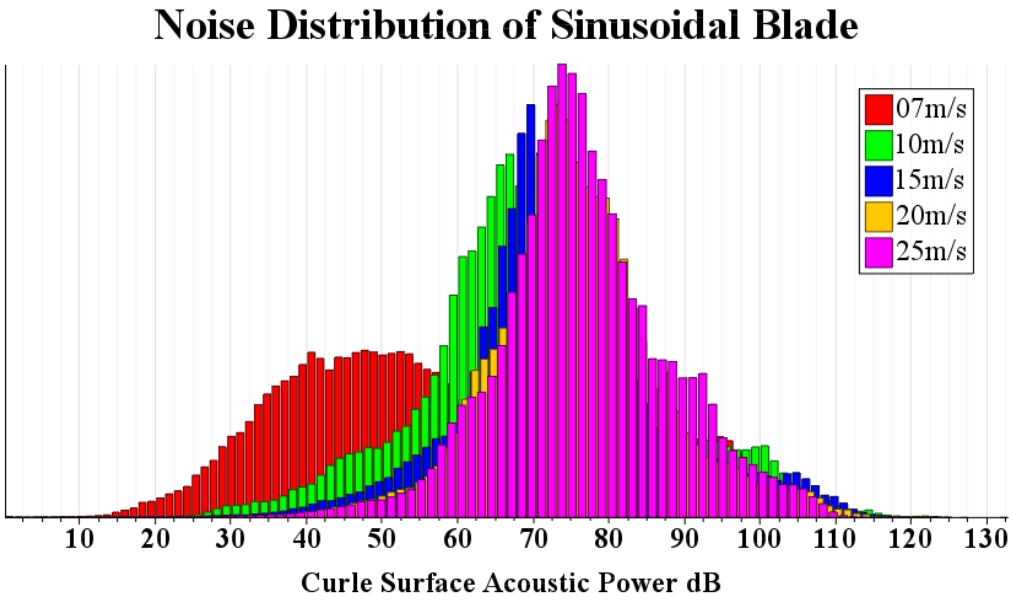

Figure 64 Noise frequency distribution at various speeds, Sinusoidal Blade

A stalled flow, as discussed in section 1.5.2 can create a lot of noise and this can be observed in Figure 63 where the average noise raises from 59.5dB at 10m/s to 65.7dB at 15m/s at which speeds flow gradually stalls along the spanwise direction. This trend is observed much earlier in a modified blade between the speeds of 7m/s and 10m/s where the leading-edge protuberances cause a disturbance in the flow and lead to separation.

7. Conclusion and Future Recommendations

The aim of this project is to compare the aerodynamic and acoustic performance of a regular NREL Phase VI wind turbine with a wind turbine with a sinusoidal leading edge and to understand the flow behavior on the blade surface. This is achieved by performing numerical analysis on both turbine models using STAR CCM+, a commercial CFD Software. Since the turbine only has two blades, taking advantage of the symmetry, only one blade is simulated instead of two and a periodic boundary condition is used. The flow is solved using RANS equations using SST κ-ω model and pressure results from the analysis are used as an input to Curle broadband noise model to predict noise sources on the blade. A mesh independence study is performed to ensure solution accuracy and optimize the computational time. To further reduce computation cost and time, only one blade is analyzed instead of two by using periodic boundary condition and use of a rotating reference frame eliminated the need of sliding mesh. All these practices help in saving time while maintaining solution accuracy.

A steady-state analysis is carried out on two blade models at wind speeds of 7 m/s, 10 m/s, 15 m/s, 20 m/s and 25 m/s. Parameters that are monitored include blade torque, blade bending moment and coefficient of pressure at five span locations. The initial analysis is performed on baseline blade and the above mentioned parameters were compared with experimental results from [11] and previous published numerical results from [27] [17] [5] to validate the model. After achieving good agreement with the other references, the same model is used to perform analysis on the modified blade. After performing numerical analysis on both the blades, it is observed that compared to the baseline blade, wind turbine with modified blade generate less torque at low wind speeds and generate more torque at high wind speeds. This behavior is attributed to the presence of tubercles on the leading edge, where at high wind speeds, the tubercles create counter-rotating

vortices at the trough which energizes the boundary layer and delay the flow separation. But on the contrary, at low wind speeds the tubercles can cause a disturbance in the laminar flow and can lead to early flow separation. The results from the noise analysis show that at wind speeds of 20 m/s and 25 m/s there is no significant difference in the noise generated by both the blades but at 15 m/s the modified blade produce relatively less noise than the baseline blade at low wind speeds the baseline blade is less noisy.

To further continue present work, unsteady CFD analysis can be performed on the models to evaluate the time-based performance of the wind turbine. The unsteady analysis also helps in understanding the noise performance of the turbine in detail. Ffowcs-Williams and Hawkings noise model can be used to evaluate the far field noise performance and can evaluate Thickness, Loading and Quadruple noise generated by both the models and comparison can be made to identify relative noise performance of both the models.

8. References

[1] F. Fish and J. Battle , "Hydrodynamic design of the humpback whale flipper," *Journal of Morphology,* vol. 225, no. 1, pp. 51-60, 1995.

[2] D. miklosovic, M. Murray, L. E. Howle and F. E. Fish , "Leading-edge tubercles delay stall on humpback whale (Megaptera novaeangliae) flippers," *Physics of Fluid,* vol. 16, no. 5, pp. 39-41, 2004.

[3] H. T., "Whale-inspired wind turbines," MIT Technology Review, 6 March 2008.

[4] T. Pecock and E. Bradley , "Going with (or against) the flow," *Science,* pp. 320:1302-1303, 2008.

[5] R.-K. Zhang and J.-Z. Wu, "Aerodynamic Charecteristics of wind turbine blades with a sinusoidal leading edge," *WIND ENERGY,* pp. 407-424, 2012.

[6] G. Abate and D. N. Navris, "CFD Analysis of Leading Edge Tubercle Effects on Wind Turbine Performance," *AIAA Propulsion and Energy Forum,* pp. 1-17, 2017.

[7] A. Corsini, G. Delibra and A. G. Sheard, "On the role of Leading-edge Bumps in the control of stall onset in Axial Fan Blades," *Fluids Engineering,* vol. 135, p. 9, 2013.

[8] "http://needtoknow.nas.edu/energy/," The national Academies of Sciences Engineering Medicine, 2015. [Online]. [Accessed 2018].

[9] D. Shepherd, D. Welch, E. Hill, D. Mcbribe and K. Dirks, "Evaluationg the Impact of Wind Turbine Noise on Health-related Quality of Life," *Noise and Health,* vol. 13, no. 54, 2011.

[10] H. Klug, "Noise from Wind Turbines: Standards and Noise Reduction Procedures," *Paper presented on the Forum Acusticum, Sevilla, Spain,* pp. 16-20, 2002.

[11] M. Hand, D. Simms, L. Fingersh, D. Jager, J. Cotrell, S. Schreck and S. Larwoos, *Unsteady Aerodynamics Experiment Phase VI: Wind Tunnel Test Configurations and Available Data Campaigns,* NREL/TP-500-29955, 2001.

[12] US Energy Information Administration , "Monthly Energy Review," U.S. Department of Energy, Washington D.C, 2018.

[13] A. Das and P. K. Talapatra, "Modelling and Analysis of a Mini Vertical Axis Wind Turbine," *International Journal of Emerging Technology and Advanced Engineering,* vol. VI, no. 6, pp. 184-194, 2016.

[14] Y. Ji, "Looking inside Wind Turbine," 02 October 2015. [Online]. Available: https://medium.com/@youngji/looking-inside-wind-turbine-9e2888fb2ee. [Accessed 15 August 2018].

[15] H. Beem and M. Triantafyllou, "Exquisitely sensitive seal whisker-like sensors detect wakes at large distances".

[16] S. Wagner , R. Bareib and G. Guidati , Wind Turbine Noise, Springer, 1996.

[17] E. Sagol, M. Reggio and A. Ilinca, "Assessment of Two-Equation Turbulence Models and Validation of the Performance Characteristics of an Experimental Wind Turbine by CFD," *ISRN Mechanical Engineering,* pp. 1-10, 2012.

[18] M. Ghasemain and A. Nejat, "Aerodynamic noise prediction of a Horizontal Axis Wind Turbine using Improved Delayed Detached Eddy Simulation and acoustic analogy," *Energy Conversion and Management 99,* pp. 210-220, 2015.

[19] A. Tadamasa and M. Zangeneh, "Numerical Prediction of Wind Turbine Noise," *Renewable Energy 36,* pp. 1902-1912, 2011.

[20] M. Asli, B. M. Gholamali and A. M. Tousi, "Numerical Analysis od Wind Turbine Airfoil Aerodynamic Performance With Leading Edge Bump," *Mathematical Problems in Engineering,* p. 8, 2015.

[21] M. Peric and S. Ferguson, *The advantage of polyhedral meshes,* CD-adapco.

[22] Star CCM+ Documentation , "Star CCM+ 12.04.011 -R8".

[23] "SST K-Omega Model," STAR CCM+, [Online]. Available: https://documentation.thesteveportal.plm.automation.siemens.com/starccmplus_latest_en/index.html#page/STARCCMP/GUID-14F1432B-B915-42FE-9862-71D1B53BEA6B=en=.html. [Accessed August 2018].

[24] F. R. Menter, "Two-equation eddy-viscosity turbulence modeling for engineering applications," *AIAA,* vol. 32, no. 8, pp. 1598-1605, 1994.

[25] *ANSYS fluent 12.0 theory guide.*

[26] wisler, 2000.

[27] N. Sorensen, J. Michelsen and S. Schreck, "Navier- Strokes Predictions of the NREL Phase VI Rotor in the NASA Ames 80 ft x 120 ft Wind Tunnel," *Wind Energy,* pp. 5:151-169, 2002.

[28] N. Rostamzadeh, K. Hansen, R. Kelso and B. B. Dally, "The formation mechanism and impact of streamwise vortices om NACA 0021 airfoil's performance with undulating leading edge modification," *Physics of Fluid 26,* pp. 1-22, 2014.

[29] M. Maizi, M. Mohamed, R. Dizene and M. Mihoubi, "Noise reduction of a horizontal wind turbine using different blade shapes," *Renewable Energy 117,* pp. 242-256, 2018.

[30] T. Hansen and L. Enggaard, *Sound Power measurements according to IEC 61400-11,* Siemens Wind Power A/S, 2012.

[31] R. Giridhar, "Prediction of Aerdynamic Noise Generated by Wind Turbine Blades," Lawrence, KS, 2016.

[32] C. Cai, Z. Zuo, T. Maeda, Y. Kamada and Q. Li, "Periodic and aperiodic flow patterns around an airfoil with leading-edge protuberances," *Physics of Fluids 29*, p. 14, 2017.

[33] J. Muyskens, D. Keating and s. granados, "Mapping how the United States generates its electricity," The Washington Post , 28 March 2017. [Online]. Available: https://www.washingtonpost.com/graphics/national/power-plants/?noredirect=on&utm_term=.63ce242e63b8. [Accessed 15 August 2018].